SOLUTION OF FULLY-COUPLED SHALLOW WATER EQUATIONS AND CONTAMINANT TRANSPORT USING A PRIMITIVE VARIABLE RIEMANN SOLVER AND A SEMI-DISCRETE SUPG METHOD

By

Faranak Behzadi

James C. Newman III
Professor of Computational Engineering
(Chair)

William K. Anderson
Professor of Computational Engineering
(Committee Member)

W. Roger Briley
Professor of Computational Engineering
(Committee Member)

John V. Matthews III
Associate Professor of Mathematics
(Committee Member)

SOLUTION OF FULLY-COUPLED SHALLOW WATER EQUATIONS AND CONTAMINANT TRANSPORT USING A PRIMITIVE VARIABLE RIEMANN SOLVER AND A SEMI-DISCRETE SUPG METHOD

By

Faranak Behzadi

A Dissertation Submitted to the Faculty of the University of Tennessee at Chattanooga in Partial Fulfillment of the Requirements of the Degree of Doctor of Philosophy in Computational Engineering

The University of Tennessee at Chattanooga
Chattanooga, Tennessee

May 2016

ABSTRACT

In the present dissertation, a finite volume and a finite element model are developed and tuned for the solution of the fully-coupled two-dimensional Shallow Water and Contaminant transport Equations with arbitrary bed topography and wetting-drying fronts. A Riemann-solver finite volume scheme, using primitive variables rather than conserved variables, and a semi-discrete Streamline Upwind Petrov-Galerkin (SUPG) method in finite element context are applied to compare the performance of these two numerical models. The Riemann-solver scheme is based on the unstructured finite volume discretization using primitive-variable Roe-flux approximation with an entropy fix. Second-order accuracy in space and time, an implicit scheme based on Newton-iterative algorithm, and an Euler explicit scheme are applied for the finite volume model. For the SUPG finite element model, a new exact source-term balancing method is introduced in this study. This new balancing method satisfies the C-property for both still water and dry regions on a non-flat bed. Two different stabilization terms are applied to compare their performance for wet-bed problems and a shock-capturing scheme is implemented to accommodate shock wave fronts. Linear triangular elements are used to decompose the computational domain and a second-order backward differentiation (BDF2) implicit method is used for the time integration. The resulting nonlinear system is solved using a Newton-type method where the linear system is solved at each step using the Generalized Minimal Residual (GMRES) algorithm. Both finite volume and finite element formulations are applied to moving-boundary problems on fixed numerical meshes. In

order to examine the accuracy and robustness of the present scheme to predict the flow variables and contaminant transport, numerical results are verified by several test cases. These cases include wet and dry dam break problems, evolution of a dam break wave with an obstacle downstream of the dam, oscillation of a bead of water in a parabolically-shaped basin, supercritical flow in a constricted channel, as well as advection and diffusion of contaminant with the flow. The scenario of contaminant transport in a notional river is also simulated to demonstrate that the present work can be implemented on practical applications involving flooding and contaminant transport.

DEDICATION

This dissertation is dedicated to my amazing husband, whose love is a great gift in my life, my loving mother, who made me who I am and fills my life with her love, encouragement and prayers, my dear father, who has taught me to be a strong woman, and my precious sisters, for their love and for encouraging me to believe in myself.

ACKNOWLEDGEMENTS

I would like to express my sincere appreciation to my adviser, Prof. James C. Newman III. His guidance, encouragement and continuous support will forever be appreciated. Without his help, this dissertation would not have been completed. I wish to express my heartfelt gratitude to Prof. Timothy W. Swafford, for giving me the opportunity of studying in the SimCenter and for his support and kindness along the way. I would also like to thank my committee members, Prof. W. Roger Briley, Prof. W. Kyle Anderson and Prof. John V. Mathews III, for their help and advice. I also wish to thank Dr. Emily R. Averitt, who helped me find courage in my life and go through the hard times. I will forever be grateful to her. Last but not least I am thankful to my friends and colleagues at the SimCenter. Arash Ghasemi, Bruce Hilbert and Ethan Hereth deserve special mention.

TABLE OF CONTENTS

LIST OF TABLES

LIST OF FIGURES

LIST OF SYMBOLS

x, y, Cartesian coordinates

h, water depth

h_s, bottom elevation measured from the still-water surface

ζ, free-surface elevation

u, depth-averaged velocity component in x-direction

v, depth-averaged velocity component in y-direction

ϕ, depth-averaged contaminant concentration

Q, vector of conserved variables

q, vector of primitive variables

F, inviscid flux vector in x-direction

G, inviscid flux vector in y-direction

S, source vector

τ_{bx}, frictional stress on the bottom in x-direction

τ_{bx}, frictional stress on the bottom in y-direction

K, empirical dispersion matrix

C, Chezy number

R, hydraulic radius

i, j, Cartesian unit vectors

Ω, area of computational domain

dA, differential area of Ω

dl, differential length of $\partial\Omega$

M, transformation matrix for change of variables

A, B, flux Jacobian matrices

W, characteristic variable

Δt, time step

V, area of control volume

ψ_k, Lagrangian basis functions at node k

npe, number of nodes per each element

J, Jacobian of transformation

W, continuous weighting-function defined over the domain

nel, number of elements

δ_s, stabilization parameter

ν_{shock}, shock-capturing parameter

W_k, basis function associated with node k

c, acoustic speed

U, velocity vector

$\tilde{h}_s$, modified bottom topography

CHAPTER 1

INTRODUCTION

Due to the wide range of engineering applications, finding effective and accurate numerical methods to solve the shallow water equations (SWEs) has been of increasing interest in the last decades. Since pollutant dispersion in rivers and coastal regions has serious impact on the ecology, environment and the human health, the two-dimensional shallow water model has become an important field of study to predict advection-diffusion of contaminants in free surface flows. In some works [1, 2] the contaminant transport equation is solved using a decoupled algorithm; that is, after solving the shallow water equations for the flow variables, the contaminant in the flow field is computed. These approaches may lead to inaccurate solutions in some cases, e.g., when the flow rapidly changes in time or in space [3]. In order to improve accuracy and robustness, a fully-coupled model should be implemented that preserves conservation and prevents numerical instabilities. The resulting system is a hyperbolic system of coupled nonlinear partial differential equations. Numerically solving this system is very challenging due to difficulties associated with discontinuities, irregular bed topography, bed roughness, and wetting-drying fronts.

Preserving the still-water condition for arbitrary bed topography is one of the challenges encountered when solving the system of shallow water equations. A well-balanced numerical scheme should satisfy the C-property [4], which requires that the quiescent state is preserved through exactly balancing the source term and numerical flux.

Another difficulty in simulating shallow water flows is accurately modeling the wetting-drying fronts. To represent the transition from wet to dry, the numerical scheme should preserve mass and momentum conservation near dry-wet fronts. There are four types of wetting-drying (WD) algorithms which are described in [5]. Various numerical methods along with WD algorithms have been developed to address these challenges and simulate the free surface flows and contaminant transport properly.

The purpose of this work is to simulate unsteady free surface flows and obtain a reliable estimation of pollution dispersion in such flows. To this end, a Finite Volume (FV) method and a Finite Element (FE) scheme are applied to the Shallow Water and Contaminant-transport Equations (SWCEs). The present finite volume scheme is based on the primitive variables Roe-flux approximation. In finite element framework, a semi-discrete Streamline Upwind Petrov-Galerkin (SUPG) is also developed. Numerical solutions for flow variables as well as pollutant transport are compared for both schemes.

1.1 Two-Dimensional Shallow Water and Contaminant Transport Equations

The two-dimensional shallow water equations are obtained from depth averaging the incompressible Navier-Stokes equations, assuming that the pressure is hydrostatic and vertical acceleration is negligible. In this work, viscosity, turbulence, wind effects, and Coriolis terms are omitted. To satisfy still-water equilibrium in the presence of a non-flat bed, Rogers et al. [6, 7] presented a particular formulation based on the free surface elevation $\zeta(x, y, t)$. As shown in Figure (1.1), the

free surface elevation may be written as

$$\zeta(x, y, t) = h(x, y, t) - h_s(x, y) \tag{1.1}$$

where h is the water height and h_s is the bottom elevation measured from the still-water surface. Sivakumar et al. [8] have used a formulation similar to that of Rogers [6, 7]. This special form of the equations satisfies still-water equilibrium and allows for possible dry regions. In this study, the formulation in [8] is used and coupled with the depth averaged scalar transport equation. The resulting system of nondimensional SWCEs for two-dimensional problems may be written in conservative form as

$$\frac{\partial Q}{\partial t} + \frac{\partial F(Q)}{\partial x} + \frac{\partial G(Q)}{\partial y} + S(Q) = 0 \tag{1.2}$$

The vector of conserved variables (Q), the inviscid flux vectors (F, G) and the source vector (S) are defined by

$$Q = \begin{Bmatrix} h \\ h\,u \\ h\,v \\ h\,\phi \end{Bmatrix} \quad F = \begin{Bmatrix} h\,u \\ h\,u^2 + \frac{1}{2}(h^2 - h_s^2) \\ h\,u\,v \\ h\,u\,\phi \end{Bmatrix} \quad G = \begin{Bmatrix} h\,v \\ h\,u\,v \\ h\,v^2 + \frac{1}{2}(h^2 - h_s^2) \\ h\,v\,\phi \end{Bmatrix} \tag{1.3}$$

$$S = \begin{Bmatrix} 0 \\ -(h - h_s)\frac{\partial h_s}{\partial x} + \tau_{bx} \\ -(h - h_s)\frac{\partial h_s}{\partial y} + \tau_{by} \\ -\nabla.\,(\mathrm{K}h\nabla\phi) \end{Bmatrix} \tag{1.4}$$

where the empirical dispersion matrix is expressed as [3]

$$\mathrm{K} = \begin{bmatrix} K_{xx} & K_{xy} \\ K_{yx} & K_{yy} \end{bmatrix} \tag{1.5}$$

Thus, the contaminant transport source term can be written as

$$\nabla.\,(\mathrm{K}h\nabla\phi) = \frac{\partial}{\partial x}\left[h\left(K_{xx}\frac{\partial\phi}{\partial x} + K_{xy}\frac{\partial\phi}{\partial y}\right)\right] + \frac{\partial}{\partial y}\left[h\left(K_{yx}\frac{\partial\phi}{\partial x} + K_{yy}\frac{\partial\phi}{\partial y}\right)\right] \tag{1.6}$$

In the present work, bottom friction stresses are computed using the Chezy model [9] and the Manning coefficient n as follows

$$C = \frac{R^{1/6}}{n} \tag{1.7}$$

$$\tau_{bx} = \frac{g\,u\,\sqrt{u^2 + v^2}}{C^2} \tag{1.8}$$

$$\tau_{by} = \frac{g\,v\,\sqrt{u^2 + v^2}}{C^2} \tag{1.9}$$

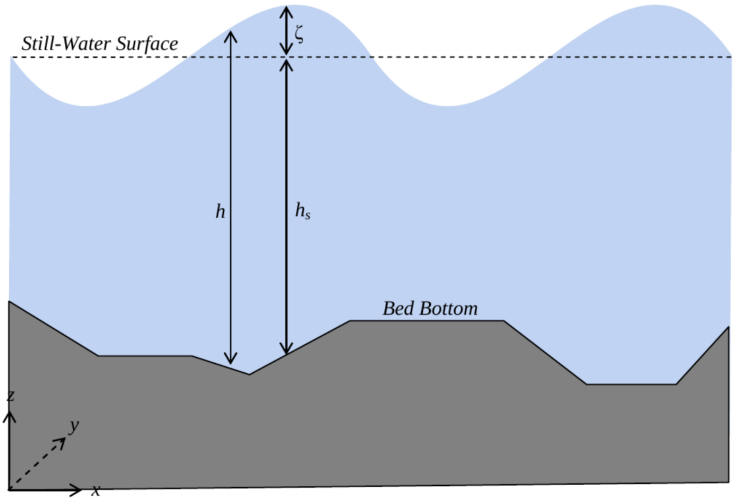

Figure 1.1 Definitions of free surface variables in shallow water problems

1.2 The Finite Volume Method

Among different numerical schemes, finite volume methods have been extensively applied to simulate SWCEs, primarily due to the mass conservation property and lower memory requirements [10]. Different finite volume methods for shallow water equations are presented in [11]. Some of these methods are numerically unstable and produce oscillatory solutions. These undesirable effects result from the flux gradients and source terms not being well-balanced. There are many numerical treatments of source-term presented in the literature to accurately solve either SWEs [8, 12–19] or coupled SWCEs [3, 20–25]. Li et al. [3] developed a fully-coupled model of shallow water flows and pollutant transport using a second-order upwind finite volume method. In that work, the HLL Riemann-solver and an explicit-implicit time integration method was used. Murillo et al. [20, 21] applied an explicit first-order upwind scheme to solve the coupled shallow water equations and pollutant transport using Roe fluxes. An approximated flux Jacobian matrix is defined in their work to treat the source term for arbitrary bed slopes. Murillo et al., also presented a finite volume

model in [22] to simulate convection and diffusion of solute transport in shallow water flows over variable bottom topography. These researchers applied a first-order upwind technique, a second order in space and time and an extended first-order method to solve the non-diffusive terms in both the flow and solute equations, and a centered implicit discretization to the diffusion terms. Lorenzo et al. [23] utilized a cell-centered finite volume method to solve the shallow water flow and scalar transport with tracking of the fluid volume and the free surface elevation in partially wet cells in order to deal with stationary or moving wet/dry fronts. Benkhaldoun et al. [24] developed a finite volume non-homogeneous Riemann solver for pollutant transport by shallow water equations using upwind fluxes and slope limiters. In that work, the pollutant concentration was used as a monitoring function for mesh refinements. Cea and Cendon [25] proposed an unstructured upwind finite volume discretization for the bed friction term in two-dimensional shallow water equations in which the bed friction is a relevant force in the momentum equation.

1.3 The Finite Element Method

Because of its geometric flexibility and high accuracy, the finite element method has also been applied to the shallow water equations [26–37], . Introducing high-order schemes in finite element models is straightforward. Additionally, Neumann boundary conditions are imposed naturally in finite element algorithms. Both the standard Continuous Galerkin (CG) and the Discontinuous Galerkin (DG) methods have been employed to solve the shallow water equations.

Bunya et al. [26] proposed a wetting and drying treatment for a Runge-Kutta Discontinuous Galerkin approximation to the SWEs. Lai [32] also developed a DG finite element method using the HLLC Riemann solver to calculate the numerical fluxes. Xing [33] used a high-order DG

method for SWEs on unstructured triangular meshes, while maintaining the still water steady state exactly and preserving the non-negativity of the water height without loss of mass conservation.

The standard Continuous Galerkin method works properly when diffusion dominates, but it produces spurious oscillations in the solution for convection-dominated problems. In order to improve the stability and convergence of the CG method, Brooks and Hughes [38] introduced the Streamline Upwind Petrov-Galerkin (SUPG) method for incompressible flows. In the SUPG method, the standard Galerkin weighting functions are modified by adding a streamline upwind perturbation to the formulation. The SUPG formulation for compressible flows was originally introduced by Tezduyar and Hughes in [39–41]. SUPG is an accurate method for problems with smooth solutions, but typically introduces localized oscillations about discontinuities [42]. To improve this behavior, a discontinuity-capturing term should be added to the formulation to provide stability near the shock fronts to enhance the robustness. For the SWEs many developments have utilized the SUPG scheme in conjunction with the stabilization and shock-capturing terms. Bova and Carey [43] presented a symmetric form of the shallow water conservation system which can be discretized using SUPG method previously proposed for a symmetric form of the Euler equation [44]. Heniche et al. [31] developed a CG finite element model which accepts positive and negative values for the water depth. Takase et al. [27] presented a space-time SUPG formulation for the SWEs using the stabilization and shock-capturing parameters based on the model applied to the Navier-Stokes equations in [45–47]. Takase et al. [28] also developed a space-time SUPG method which combines a stabilization parameter, a compressible-flow shock-capturing parameter adapted for shallow-water flows, and remeshing. Zhao et al. [29] used a well-balanced two-step

Taylor-Galerkin scheme with a local bed slope modification in wetting-drying interfaces. Porta et al. [30] provided a space-time adaptation scheme which permits separate space and time adaptation.

A finite element model may be implemented using either a moving or a fixed computational grid to accommodate wetting-drying problems. Bates and Horritt [48] presented different moving and fixed grid models. Deforming mesh schemes for moving boundary problems involves tracking the exact location of the shoreline, relocating grid points and testing for mesh quality at each time step. However, this approach results in an inefficient procedure. Bates and Hervouet [49] presented a finite element algorithm to solve moving-boundary problems on fixed numerical grids, and consists of identifying partly wet elements, canceling spurious water-surface slope terms in the momentum equations and rescaling the continuity equation to represent the true volume of water on the partly wet elements. Aizinger and Dawson [34] described a DG scheme for the SWECs, and Caleffi and Valiani [50] applied a third-order local DG method to the mathematical model of passive contaminant transport in open-channel flows.

1.4 The Present Methods

The first purpose of the current research is to extend Sivakumar's algorithm [8] to develop a robust finite volume model for solving fully-coupled SWCEs. Sivakumar et al. [8] presented a modified Roe scheme with an exact source-term balancing method in order to develop a well-balanced and well-behaved algorithm dealing with non-uniform bed topography and dry regions. The present scheme is based on the unstructured finite volume discretization for the fully-coupled SWCEs system, using primitive variable Roe-flux approximation with an entropy fix. Second-order

accuracy in space and time, nonlinear implicit and Euler explicit schemes are applied in the present finite volume method.

Secondly, a new well-balanced finite element model is developed based on semi-discrete SUPG method to solve the two-dimensional fully-coupled SWCEs with the ability to accurately resolve wetting-drying fronts on arbitrary bed topography. The formulation used in a finite volume algorithm [8] is now introduced into the finite element framework. Having discussed the disadvantage of deforming mesh schemes, simulations are carried out on a fixed computational grid using an Eulerian method. A discretization for a non-flat bottom is introduced for the first time in the finite element framework to balance the discrete flux gradients and source term for both still water and dry regions. Linear second-order triangles are used to decompose the computational domain. Moreover, this methodology can be easily extended to higher order elements. Implicit time integration using the second-order backward difference (BDF2) scheme is utilized.

1.5 Outline

In the remaining chapters, the details of developed numerical algorithms for fully-coupled SWCEs are described. Chapter 2 presents the mathematical model of the applied finite volume method. In Chapter 3, the implemented SUPG model and the new exact source-term balancing scheme is explained in detail. Results from several numerical test cases are discussed in Chapter 4. Finally, conclusions and recommendations for future work are summarized in Chapter 6.

CHAPTER 2

FINITE VOLUME METHODOLOGY

This chapter describes the finite volume discretization for the SWCEs utilized in the current work. Additionally, implementation issues are discussed in detail.

2.1 Finite Volume Discretization and Primitive-Variable Roe-Flux for SWCEs

The integral form of equation (1.2) over an arbitrary fixed domain Ω enclosed by $\partial\Omega$, is given by

$$\frac{\partial}{\partial t}\int_{\Omega} Q\, dA + \oint_{\partial\Omega} E.\boldsymbol{n}\, dl + \int_{\Omega} S\, dA = 0 \tag{2.1}$$

where $E = F\,\hat{i} + G\,\hat{j}$ and $\boldsymbol{n}$ is defined as an outward unit normal vector. The spatial domain Ω is divided into triangular cells and a node-centered finite volume scheme is developed based on the median dual control volume as shown in Figure (2.1). The surface flux integral for node i and its neighbor node j may be written as

$$\oint_{\partial\Omega} E.n\, dl \approx \sum_{j\in N(i)} H_{ij} \tag{2.2}$$

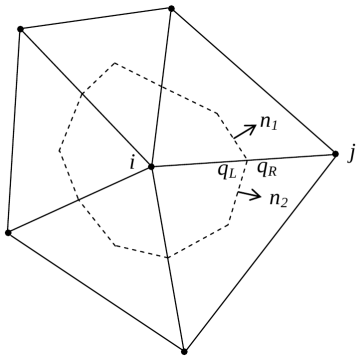

Figure 2.1 Illustration of a median dual control volume

Defining $\theta = u\,n_x + v\,n_y$, the flux function H in (2.2) for SWCEs is given by

$$H = E.n\,dl = F.n_x + G.n_y = \left\{ \begin{array}{c} h\,\theta \\ h\,u\,\theta + \frac{1}{2}(h^2 - h_s^2)n_x \\ h\,v\,\theta + \frac{1}{2}(h^2 - h_s^2)n_y \\ h\,\phi\,\theta \end{array} \right\} \tag{2.3}$$

Therefore, the flux Jacobian for SWCEs based on equation (2.3) is obtained as

$$\frac{\partial H}{\partial Q} = A_H = \left[\begin{array}{cccc} 0 & n_x & n_y & 0 \\ -u^2 n_x - u\,v\,n_y + n_x h & 2\,u\,n_x + v\,n_y & u\,n_y & 0 \\ -v^2 n_y - u\,v\,n_x + n_y h & v\,n_x & u\,n_x + 2v\,n_y & 0 \\ -n_x u\,\phi - n_y v\,\phi & \phi\,n_x & \phi\,n_y & u\,n_x + v\,n_y \end{array} \right] \tag{2.4}$$

In the present study to construct a stable scheme, the flux function utilizes Roe fluxes and is approximated based on the primitive-variable vector defined as $q = \{h\ u\ v\ \phi\}^T$. The transformation

matrix M for change of variables from conservative to primitive form is given in (2.5).

$$M = \frac{\partial Q}{\partial q} = \begin{bmatrix} 1 & 0 & 0 & 0 \\ u & h & 0 & 0 \\ v & 0 & h & 0 \\ \phi & 0 & 0 & h \end{bmatrix} \qquad M^{-1} = \begin{bmatrix} 1 & 0 & 0 & 0 \\ -\frac{u}{h} & \frac{1}{h} & 0 & 0 \\ -\frac{v}{h} & 0 & \frac{1}{h} & 0 \\ -\frac{\phi}{h} & 0 & 0 & \frac{1}{h} \end{bmatrix} \tag{2.5}$$

Using the primitive variables q, equation (1.2) can be written as

$$\begin{aligned} \frac{\partial Q}{\partial t} + \frac{\partial F(Q)}{\partial x} + \frac{\partial G(Q)}{\partial y} + S(Q) &= M\frac{\partial q}{\partial t} + AM\frac{\partial q}{\partial x} + BM\frac{\partial q}{\partial y} + S(q) \\ &= \frac{\partial q}{\partial t} + a\frac{\partial q}{\partial x} + b\frac{\partial q}{\partial y} + M^{-1}S(q) = 0 \end{aligned} \tag{2.6}$$

where $A = \frac{\partial F}{\partial Q}$, $B = \frac{\partial G}{\partial Q}$, $a = M^{-1}AM$, and $b = M^{-1}BM$. Thus, the flux Jacobian for the primitive variables a_H is defined as

$$a_H = M^{-1}A_H\,M = \begin{bmatrix} \theta & h\,n_x & h\,n_y & 0 \\ n_x & \theta & 0 & 0 \\ n_y & 0 & \theta & 0 \\ 0 & 0 & 0 & \theta \end{bmatrix} \tag{2.7}$$

To evaluate a conservative and well-behaved flux at each control-volume interface, the primitive-variable Roe scheme is applied as

$$H_{ij} = \frac{1}{2}\left[(H_L + H_R) - |A_H|\,M\,(q_R - q_L)\right] = \frac{1}{2}\left[(H_L + H_R) - M\,|a_H|\,(q_R - q_L)\right] \tag{2.8}$$

where M and a_H are evaluated at Roe-averaged values given by

$$\begin{aligned} h &= \tfrac{1}{2}\left(h_L + h_R\right) \\ u &= \tfrac{u_L\sqrt{h_L}+u_R\sqrt{h_R}}{\sqrt{h_L}+\sqrt{h_R}} \\ v &= \tfrac{v_L\sqrt{h_L}+v_R\sqrt{h_R}}{\sqrt{h_L}+\sqrt{h_R}} \\ \phi &= \tfrac{\phi_L\sqrt{h_L}+\phi_R\sqrt{h_R}}{\sqrt{h_L}+\sqrt{h_R}} \end{aligned} \tag{2.9}$$

To obtain the flux dissipation matrix $M\,|a_H|$ in equation (2.8), eigenvalues and eigenvectors of a_H are required. Since A_H and a_H are similar matrices, they have the same set of eigenvalues which are $\lambda_k = \left(\theta,\, \theta,\, \theta + \sqrt{h},\, \theta - \sqrt{h}\right)$. The diagonal matrix of eigenvalues, as well as right and left eigenvectors of a_H, are given in equations (2.10) to (2.12).

$$|\Lambda| = \begin{bmatrix} |\lambda_1| & & & \\ & |\lambda_2| & & \\ & & |\lambda_3| & \\ & & & |\lambda_4| \end{bmatrix} = \begin{bmatrix} |\theta| & & & \\ & |\theta| & & \\ & & \left|\theta + \sqrt{h}\right| & \\ & & & \left|\theta - \sqrt{h}\right| \end{bmatrix} \tag{2.10}$$

$$R_q = \begin{bmatrix} 0 & 0 & 1 & 1 \\ \frac{-n_y}{h} & 0 & \frac{n_x}{\sqrt{h}} & \frac{-n_x}{\sqrt{h}} \\ \frac{n_x}{h} & 0 & \frac{n_y}{\sqrt{h}} & \frac{-n_y}{\sqrt{h}} \\ 0 & 1 & 0 & 0 \end{bmatrix} \tag{2.11}$$

$$R_q{}^{-1} = \begin{bmatrix} 0 & -h\,n_y & h\,n_x & 0 \\ 0 & 0 & 0 & 1 \\ \frac{1}{2} & \frac{n_x\sqrt{h}}{2} & \frac{n_y\sqrt{h}}{2} & 0 \\ \frac{1}{2} & \frac{-n_x\sqrt{h}}{2} & \frac{-n_y\sqrt{h}}{2} & 0 \end{bmatrix} \tag{2.12}$$

Thus, the flux dissipation matrix of Roe approximation in (2.8) is given by

$$M\,|a_H| = M\,R_q\;|\Lambda|\;R_q{}^{-1} = \frac{1}{2}\begin{bmatrix} \beta^+ & n_x\sqrt{h}\,\beta^- & n_y\sqrt{h}\,\beta^- & 0 \\ u\,\beta^+ + n_x\sqrt{h}\,\beta^- & u\,n_x\sqrt{h}\,\beta^- + \Psi_1 & u\,n_y\sqrt{h}\,\beta^- + \Psi_2 & 0 \\ v\,\beta^+ + n_y\sqrt{h}\,\beta^- & v\,n_x\sqrt{h}\,\beta^- + \Psi_2 & v\,n_y\sqrt{h}\,\beta^- + \Psi_3 & 0 \\ \phi\,\beta^+ & n_x\phi\,\sqrt{h}\,\beta^- & n_y\phi\,\sqrt{h}\,\beta^- & h\,|\lambda_1| \end{bmatrix} \tag{2.13}$$

where

$$\begin{aligned} \beta^+ &= |\lambda_3| + |\lambda_4| \\ \beta^- &= |\lambda_3| - |\lambda_4| \\ \Psi_1 &= h\,n_x{}^2\beta^+ + 2\,h\,|\lambda_1|\,n_y{}^2 \\ \Psi_2 &= h\,n_x n_y\;(\beta^+ - 2\;|\lambda_1|) \\ \Psi_3 &= h\,n_y{}^2\beta^+ + 2\,h\,|\lambda_1|\,n_x{}^2 \end{aligned} \tag{2.14}$$

2.2 Spatial Accuracy

In the present study, second order spatial accuracy is constructed by extrapolating the nodal solutions to the faces surrounding the control volume. Nodal values and gradients are required to

evaluate q_L and q_R at each cell interface in equation (2.8) as follows

$$\begin{aligned} q_L &= q_i + \nabla q_i \cdot \boldsymbol{r}_{ij} \\ q_R &= q_j + \nabla q_j \cdot \boldsymbol{r}_{ji} \end{aligned} \tag{2.15}$$

Here i represents the center node of control volume and j is its neighbor point, as shown in Figure (2.1). $\boldsymbol{r}_{ij}$ is the vector extending from node i to the midpoint of edge ij. Either Green's theorem [51] or the least squares method discussed in [52] can be used to compute the gradients at the vertices. In the present algorithm, ∇q in (2.15) is computed via Green's theorem as follows

$$\int_{\Omega} \nabla q \, d\Omega = \int_{\partial\Omega} q \cdot n \, dA \tag{2.16}$$

Noting that the area of integration is made up of discrete pieces, the gradient at vertex i is computed as follows

$$\nabla q_i = \frac{1}{\Omega_i} \sum_{j \in N(i)} \frac{1}{2} \left(q_i + q_j \right) n_{ij} \tag{2.17}$$

where Ω_i is the area of median dual surrounding node i.

2.3 Temporal Discretization

The time derivative term appearing in equation (2.1) is approximated with a general expression given by

$$\left(V \frac{\Delta Q^n}{\Delta t} \right)_i = \left(\frac{V}{\Delta t} \right)_i \left[(1 + \psi) \left(Q_i^{n+1} - Q_i^n \right) - \psi \left(Q_i^n - Q_i^{n-1} \right) \right] \tag{2.18}$$

where n represents the time iteration. By choosing $\psi = 0$ and $\psi = \frac{1}{2}$, first and second-order time accuracy will be achieved, respectively.

2.4 Time Advancement Approach

Utilizing the temporal and spatial discretization previously discussed, equation (2.1) may be written as

$$V\frac{\Delta Q^n}{\Delta t} + R^{n+1} = 0 \tag{2.19}$$

where $R = \oint\limits_{\partial\Omega} E.\boldsymbol{n}\, dl + \int\limits_{\Omega} S\, dA$. For an implicit scheme, the nonlinear equation (2.19) must be linearized about solution q^n, and using a Newton-iterative algorithm [53] the discrete equations become

$$\left[\left(\frac{V}{\Delta t}\right)_i (1+\psi)\,\hat{M}\right]\Delta q_i^{n+1,m} + \sum_j \delta l\left[\left(\frac{\partial \mathbf{H}_{ij}}{\partial q_L}\right)^{n+1,m}\Delta q_i^{n+1,m} + \left(\frac{\partial \mathbf{H}_{ij}}{\partial q_R}\right)^{n+1,m}\Delta q_j^{n+1,m}\right] =$$
$$-\left(\left(\frac{V}{\Delta t}\right)_i\left[(1+\psi)\left(Q_i^{n+1}-Q_i^n\right) - \psi\left(Q_i^n - Q_i^{n-1}\right)\right] + \sum_j \mathbf{H}_{ij}^{n+1}\,\delta l + V_i\,\mathbf{S}^n\right) \tag{2.20}$$

In the above formulation m represents the Newton iteration, and $\Delta q_i^{n+1,m} = \left(q_i^{n+1,m+1} - q_i^{n+1,m}\right)$. It should be noted that, based on equation (2.5), the matrix M is singular for dry regions ($h = 0$) and must be replaced by $\hat{M} = M + \epsilon\, diag(0,1,1,1)$. Numerical results depend strongly on the parameter ϵ. The smaller this parameter is, the more accurately results are obtained. This indicates the necessity of using the smallest possible ϵ while still retaining solution stability.

In the current work, the resulting sparse linear system in equation (2.20) is solved at each Newton iteration using the Gauss-Seidel stationary iterative method.

2.5 Flux Jacobian Calculations

Implicit solution algorithms require the construction of flux Jacobians which can be constructed either analytically or numerically. Numerical approximations can be obtained using finite-difference or by a complex Taylor series expansion. Numerical flux Jacobians using finite-difference is estimated by perturbing each component of the solution variable by a small amount δ and calculating the difference between the flux vectors evaluated at the perturbed and unperturbed quantities. Thus, the forward finite-difference approximation for the Jacobians are defined as follows [54, 55]

$$\begin{aligned} \frac{\partial \mathbf{H}}{\partial q_L} &\approx \frac{\mathbf{H}(q_L+\delta, q_R) - \mathbf{H}(q_L, q_R)}{\delta} \\ \frac{\partial \mathbf{H}}{\partial q_R} &\approx \frac{\mathbf{H}(q_L, q_R+\delta) - \mathbf{H}(q_L, q_R)}{\delta} \end{aligned} \tag{2.21}$$

The use of complex variables to evaluate derivatives of real functions was first introduced by Squire and Trapp [56]. Subsequently, Whitfield and Taylor [57] utilized this method for Jacobian evaluation in advanced computational fluid dynamic solvers. This method can be evaluated by perturbing the independent variable in the complex plane $(q + \tilde{i}\delta)$ as

$$\begin{aligned} \frac{\partial \mathbf{H}}{\partial q_L} &= \frac{Im[\mathbf{H}(q_L+\tilde{i}\delta, q_R)]}{\delta} \\ \frac{\partial \mathbf{H}}{\partial q_R} &= \frac{Im[\mathbf{H}(q_L, q_R+\tilde{i}\delta)]}{\delta} \end{aligned} \tag{2.22}$$

where $\tilde{i}$ in the above equation denotes the imaginary number $\sqrt{-1}$. The advantage of this technique, over finite-difference estimates, is that equation (2.22) does not possess subtractive cancellation

errors and, therefore, represents an exact second-order approximation to the Jacobian. The disadvantage of using the complex variable approximation is that complex arithmetic is more computationally expensive than using real numbers. Therefore, in the present work, flux Jacobians in equation (2.20) are approximated by finite-difference numerical Jacobians with $\delta = 10^{-7}$.

2.6 Boundary Conditions

Boundary conditions in the present study are imposed by evaluating the Roe-flux approximation through those faces of the control volume which lie on the boundary, and applying the normal solution procedure to obtain flow variables. For an inviscid solid wall $\theta = u\,n_x + v\,n_y$ is set to zero in evaluating flux vector. Inflow and outflow boundaries are modeled via characteristic variable boundary conditions. The governing equations in the normal direction to the boundary η is given by

$$\frac{\partial Q}{\partial t} + \frac{\partial H}{\partial \eta} + S = 0 \tag{2.23}$$

For primitive variables q, this can be written as

$$\frac{\partial q}{\partial t} + a_H \frac{\partial q}{\partial \eta} + M^{-1} S = 0 \tag{2.24}$$

Using a similarity transformation, matrix a_H is diagonalized as $a_H = R_q \Lambda R_q^{-1}$ where Λ and R_q have been defined previously. Multiplying both sides of equation (2.24) by R_q^{-1} and evaluating R_q^{-1} at some constant conditions (R_{q0}^{-1})

$$\frac{\partial W_0}{\partial t} + \Lambda \frac{\partial W_0}{\partial \eta} + R_{q0}^{-1} M^{-1} S = 0 \tag{2.25}$$

where $W_0 = R_{q0}^{-1} q$ is the vector of characteristic variables. Since Λ is a diagonal matrix, the resulting partial differential equations in (2.25) is a decoupled system and can be written as four uncoupled scalar equation, each of which is a nonlinear wave equation. From the theory of characteristics, information propagates along characteristic lines, at speeds determined by the eigenvalues

$$\lambda_k = \frac{\partial \eta}{\partial t} \tag{2.26}$$

Therefore, equation (2.25) can be written as a total derivative

$$\frac{dW_0}{dt} + R_{q0}^{-1} M^{-1} S = 0 \tag{2.27}$$

Discretizing equation (2.27) on the boundary

$$W_{0,b} = W_{0,r} - R_{q0}^{-1} M^{-1} S \, \Delta t \tag{2.28}$$

Here $W_{0,r}$ is the characteristic variable evaluated at the appropriate reference state which is dependent on the sign of the eigenvalues on the boundary. $W_{0,b}$ refers to the boundary state, and should be calculated to obtain the solution vector q_b.

$$q_b = R_{q0} W_{0,r} - M^{-1} S \, \Delta t \tag{2.29}$$

Once q_b is known, the numerical flux on the boundary can be evaluated.

2.7 Dry Regions

As mentioned previously, there are various types of wetting-drying algorithms that have been used for moving boundary problems. In many shallow water solvers, to treat zero depth, either a small minimum depth h_{min} is applied to dry regions during the solution process, or dry cells are removed from the computational domain. Both of these procedures could introduce errors in computations of flow variables and contaminant transport.

The present primitive formulation is well behaved at $h = 0$, while all cells are included in the computational domain, and there is no need to enforce a minimum depth for dry regions. However, the time integration may produce small negative heights or negative contaminants. In order to be physically consistent, and to avoid a negative square root, negative heights and negative contaminants are reset to zero.

2.8 Source Term Balancing

The still-water state, often referred to as the *lake at rest* solution, is defined by

$$u = v = 0 \quad \text{and} \quad h - h_s = 0 \tag{2.30}$$

where u and v are velocity components, and$h$ and h_s have been defined in Figure (1.1). A well-balanced numerical scheme should satisfy the above C-property [4] through exactly balancing the source term and numerical flux. The present finite volume method satisfies the still-water equilibrium, while the source term on a dry bed is only balanced for a flat bottom. To balance the flux integral and source term for dry regions, the method introduced in [8] is implemented for a

non-flat bed. The x- and y-momentum equations for a dry non-flat bed are reduced

$$-\oint_{\partial\Omega} \frac{h_s^2}{2} n_x \, dl + \int_{\Omega} h_s \frac{\partial h_s}{\partial x} \, d\Omega \approx -\oint_{\partial\Omega} \frac{h_s^2}{2} n_x \, dl + \tilde{h}_{s1} \int_{\Omega} \frac{\partial h_s}{\partial x} \, d\Omega = 0 \tag{2.31}$$

$$-\oint_{\partial\Omega} \frac{h_s^2}{2} n_y \, dl + \int_{\Omega} h_s \frac{\partial h_s}{\partial y} \, d\Omega \approx -\oint_{\partial\Omega} \frac{h_s^2}{2} n_y \, dl + \tilde{h}_{s2} \int_{\Omega} \frac{\partial h_s}{\partial y} \, d\Omega = 0 \tag{2.32}$$

For each node, the above two scalar equations are solved for $\tilde{h}_{s1}$ and $\tilde{h}_{s2}$ to maintain an exact balance in the x- and y-directions, respectively. The calculation process of $\tilde{h}_{s1}$ and $\tilde{h}_{s2}$ is performed only once, prior to starting the solution, and these values will be used in computing the source term on all control volumes.

CHAPTER 3

FINITE ELEMENT METHODOLOGY

In this chapter, a stabilized finite element methodology based on a semi-discrete SUPG method is described and implemented into the SWCEs. Since the SUPG method is not compatible for cases with a non-flat bottom, a new algorithm for addressing wetting-drying fronts is introduced. This algorithm computes a modified bottom topography which is utilized in the source term.

3.1 Finite Element Discretization

To apply the finite element method, the computational domain is divided into non-overlapping triangular elements. The finite element approximation is expanded as a series of Lagrangian basis functions ψ_k and dependent variables $\hat{Q}_k$, for element e as

$$Q(x, y) = \sum_{k=1}^{npe} \hat{Q}_k^e \psi_k^e(x, y) \tag{3.1}$$

Basis functions are defined based on the reference triangular element ($0 \leq \xi, \eta \leq 1$). Thus, a mapping from the reference to the physical element is required. The reference-to-physical transformation and the corresponding Jacobian of transformation J for a two-dimensional element

is given by

$$x = \sum_{k=1}^{npe} \hat{x}_k^e \psi_k^e(\xi, \eta) \tag{3.2}$$

$$y = \sum_{k=1}^{npe} \hat{y}_k^e \psi_k^e(\xi, \eta) \tag{3.3}$$

$$J = \begin{bmatrix} \frac{\partial x}{\partial \xi} & \frac{\partial x}{\partial \eta} \\ \frac{\partial y}{\partial \xi} & \frac{\partial y}{\partial \eta} \end{bmatrix} \tag{3.4}$$

3.2 Streamline Upwind Petrov-Galerkin (SUPG) Discretization

The semi-discrete SUPG formulation of the governing equation (1.2) is written as

$$\int_{\Omega} W \left(\frac{\partial Q}{\partial t} + \frac{\partial F}{\partial x} + \frac{\partial G}{\partial y} + S \right) d\Omega + \sum_{e=1}^{nel} \int_{\Omega^e} \delta_s \left(\frac{\partial Q}{\partial t} + \frac{\partial F}{\partial x} + \frac{\partial G}{\partial y} + S \right) d\Omega$$
$$+ \sum_{e=1}^{nel} \int_{\Omega^e} \nu_{Shock} \left(\frac{\partial W}{\partial x} \frac{\partial Q}{\partial x} + \frac{\partial W}{\partial y} \frac{\partial Q}{\partial y} \right) d\Omega = 0 \tag{3.5}$$

where the weighting-function W is defined using the same basis functions as for the dependent variables ($W = \psi$). The second and third terms are added stabilization and shock-capturing terms, respectively. The weak form of SWCEs after integration-by-parts on a *typical element e* is given by

$$\int_{\Omega^e} W \left(\frac{\partial Q}{\partial t} + S \right) d\Omega - \int_{\Omega^e} \left(\frac{\partial W}{\partial x} F + \frac{\partial W}{\partial y} G \right) d\Omega + \int_{\Gamma^e} W \left(F \cdot n_x + G \cdot n_y \right) d\Gamma$$
$$+ \int_{\Omega^e} \delta_s \left(\frac{\partial Q}{\partial t} + \frac{\partial F}{\partial x} + \frac{\partial G}{\partial y} + S \right) d\Omega + \int_{\Omega^e} \nu_{shock} \left(\frac{\partial W}{\partial x} \frac{\partial Q}{\partial x} + \frac{\partial W}{\partial y} \frac{\partial Q}{\partial y} \right) d\Omega = 0 \tag{3.6}$$

In this study, two different definitions for the stabilization parameter δ_s are applied to evaluate the stabilization term in equation (3.6), and are denoted as δ_{s1} and δ_{s2}.

3.2.1 Stabilization Parameter δ_{s1} and Shock-Capturing Parameter ν_{shock}

The stabilization and shock-capturing parameters are defined based on [27] and evaluated using

$$\delta_{s1} = \tau_t \left(\frac{\partial W}{\partial x} A + \frac{\partial W}{\partial y} B \right) \tag{3.7}$$

$$\nu_{shock} = \tau_{shock} \left({u_{int}}^2 \right) \tag{3.8}$$

$$\tau_t = \left[\frac{1}{{\tau_1}^2} + \frac{1}{{\tau_2}^2} \right]^{-\frac{1}{2}} \tag{3.9}$$

$$\tau_1 = \left[\sum_{k=1}^{npe} \left(c \left| \frac{\nabla h}{\|\nabla h\|} \cdot \nabla W_k \right| + |U \cdot \nabla W_k| \right) \right]^{-1} \tag{3.10}$$

$$\tau_2 = \frac{\Delta t}{2} \tag{3.11}$$

$$\tau_{shock} = \tau_1 \left(\frac{\left| \nabla^2 h \right|}{\max |\nabla^2 h|} \right) \tag{3.12}$$

$$u_{int} = \sqrt{c^2 + \|U\|^2} \tag{3.13}$$

Here u_{int} represents an intrinsic velocity. To calculate $\left|\nabla^2 h\right|$ for each element, after evaluating the first derivative via Green's theorem applied in equation (2.17), the second derivative at each element is computed using basis functions

$$\nabla^2 h = \sum_{k=1}^{npe} (\nabla h)_k \, (\nabla \psi)_k \tag{3.14}$$

3.2.2 Stabilization Parameter δ_{s2}

Another definition for the stabilization parameter is taken from [58] which is defined as

$$\delta_{s2} = \left(\frac{\partial W}{\partial x} A + \frac{\partial W}{\partial y} B \right) [\tau_a] \tag{3.15}$$

Here $[\tau_a]$ is a matrix given by

$$[\tau_a] = \left(\sum_{k=1}^{npe} \left| \frac{\partial W_k}{\partial x} A + \frac{\partial W_k}{\partial y} B \right| \right)^{-1} \tag{3.16}$$

$$\left| \frac{\partial W_k}{\partial x} A + \frac{\partial W_k}{\partial y} B \right| = T \ |\Lambda| \ T^{-1} \tag{3.17}$$

T and Λ represent the matrix of right eigenvectors and diagonal matrix of eigenvalues of $\left| \frac{\partial W_k}{\partial x} A + \frac{\partial W_k}{\partial y} B \right|$, respectively. The eigensystem for SWCEs are evaluated as

$$T = \begin{bmatrix} 0 & 0 & H_a & H_a \\ -\frac{N_y}{H_a} & 0 & h\,N_x + u\,H_a & -h\,N_x + u\,H_a \\ \frac{N_x}{H_a} & 0 & h\,N_y + v\,H_a & -h\,N_y + v\,H_a \\ 0 & 1 & \phi\,H_a & \phi\,H_a \end{bmatrix} \tag{3.18}$$

$$T^{-1} = \begin{bmatrix} \frac{h\,(u\,N_y - v\,N_x)}{H_a} & \frac{-h\,N_y}{H_a} & \frac{h\,N_x}{H_a} & 0 \\ -\phi & 0 & 0 & 1 \\ \frac{H_a - \theta_a}{2\,{H_a}^2} & \frac{N_x}{2\,{H_a}^2} & \frac{N_y}{2\,{H_a}^2} & 0 \\ \frac{H_a + \theta_a}{2\,{H_a}^2} & -\frac{N_x}{2\,{H_a}^2} & -\frac{N_y}{2\,{H_a}^2} & 0 \end{bmatrix} \tag{3.19}$$

$$|\Lambda| = \begin{bmatrix} |\theta_a| & & & \\ & |\theta_a| & & \\ & & |\theta_a + H_a| & \\ & & & |\theta_a - H_a| \end{bmatrix} \tag{3.20}$$

with

$$\theta_a = u\, N_x + v\, N_y \tag{3.21}$$

$$H_a = \sqrt{h\,(N_x^2 + N_y^2)} \tag{3.22}$$

$$N_x = \frac{\partial W_k}{\partial x} \tag{3.23}$$

$$N_y = \frac{\partial W_k}{\partial y} \tag{3.24}$$

3.3 Time Integration Scheme

Equation (3.5) can be written in a differential equation form, with the discretized spatial residual R and mass matrix M, as

$$M\frac{\partial Q}{\partial t} + R(Q) = 0 \tag{3.25}$$

Applying the second-order backward difference (BDF2) scheme to (3.25), the unsteady residual is obtained as

$$R_{uns}^{n+1} = \frac{M}{\Delta t}\left(\frac{3}{2}Q^{n+1} - 2Q^n + \frac{1}{2}Q^{n-1}\right) + R\left(Q^{n+1}\right) = 0 \tag{3.26}$$

where R_{uns}^{n+1} represents the unsteady residual at time step $n+1$. The implicit scheme requires linearization of equation (3.26). The resulting linear system at each Newton iteration is solved

using the Generalized Minimal Residual (GMRES) algorithm [59] with an ILU(0) preconditioner. The linearized incremental equations may be expressed as

$$\left(\frac{\partial R_{uns}}{\partial Q}\right)^{m,n+1} \Delta Q^{m,n} = -R_{uns}^{m,n+1} \tag{3.27}$$

In the above formulation n and m denote the time iteration and Newton iteration, respectively. It should be noted that the matrix $\left(\frac{\partial R_{uns}}{\partial Q}\right)$ becomes singular for dry regions ($h = 0$) and must be replaced with $\left(\frac{\partial R_{uns}}{\partial Q}\right) + \epsilon\, diag(0, 1, 1, 1)$.

3.4 Boundary Conditions

Flux boundary conditions are strongly enforced via the surface integral in equation (3.6). For an inviscid wall, a zero normal velocity condition ($\theta = u\, n_x + v\, n_y = 0$) is imposed in the evaluation of the flux vector on the wall. Characteristic inflow and outflow conditions are applied on the appropriate boundaries.

3.5 Wetting and drying

In general, the numerical model solves SWCEs over wet regions where fluid is present. However, accommodating dry regions plays a crucial role in modeling shallow water flows with drying and flooding applications. As previously noted, the present study focuses on using fixed computational grids. Using fixed grid models to simulate moving boundary problems in a finite element framework leads to the existence of wet, dry, and partially-wet elements as shown in Figure (3.1). Mass and momentum conservation should be properly considered for all types of elements, otherwise this may lead to numerically unstable oscillations in the wetting-drying fronts.

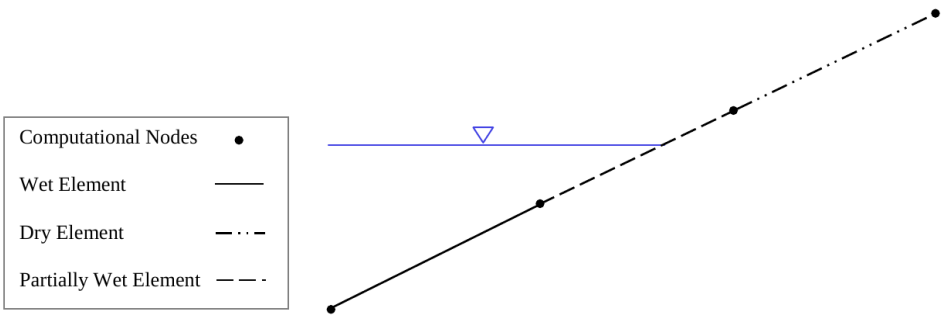

Figure 3.1 Existence of fully-wet, fully-dry, and partially-wet elements in fixed grid models

In the present work, a new algorithm is developed to accommodate dry and partially-wet elements through exactly balancing the source term and flux gradients. The algorithm is explained in details in the following section.

3.6 Exact source-term balancing

The nondimensional formulation given in equation (1.2) satisfies the still-water equilibrium for fully-wet elements in finite element discretizations and, therefore, source-term treatment should be focused on fully-dry and partially-wet elements.

3.6.1 Dry elements

The continuity equation is satisfied for a typical dry element. However, the x- and y-momentum equations reduced to

$$\int_{\Omega^e} W \frac{\partial (h\,u)}{\partial t}\, d\Omega - \int_{\Omega^e} \left[\frac{\partial W}{\partial x} \left(h\,u^2 + \frac{h^2 - h_s^2}{2} \right) + \frac{\partial W}{\partial y} h\,u\,v \right] d\Omega$$
$$+ \int_{\Gamma^e} W \left[\left(h\,u^2 + \frac{h^2 - h_s^2}{2} \right) n_x + h\,u\,v\,n_y \right] d\Gamma - \int_{\Omega^e} W \left[(h - h_s) \frac{\partial h_s}{\partial x} \right] d\Omega = 0 \quad (3.28)$$

$$\int_{\Omega^e} W \frac{\partial (h\,v)}{\partial t}\, d\Omega - \int_{\Omega^e} \left[\frac{\partial W}{\partial x} h\,u\,v + \frac{\partial W}{\partial y} \left(h\,v^2 + \frac{h^2 - h_s^2}{2} \right) \right] d\Omega$$
$$+ \int_{\Gamma^e} W \left[h\,u\,v\,n_x + \left(h\,v^2 + \frac{h^2 - h_s^2}{2} \right) n_y \right] d\Gamma - \int_{\Omega^e} W \left[(h - h_s) \frac{\partial h_s}{\partial y} \right] d\Omega = 0 \quad (3.29)$$

Note that the stabilization and shock-capturing terms, as well as friction terms, are omitted in the dry elements. Applying the dry state ($h = u = v = 0$) to equations (3.28) and (3.29) yields

$$\int_{\Omega^e} \left(\frac{h_s^2}{2} \frac{\partial W}{\partial x} \right) d\Omega + \int_{\Gamma^e} W \left(\frac{-h_s^2}{2} n_x \right) d\Gamma + \int_{\Omega^e} W \left(h_s \frac{\partial h_s}{\partial x} \right) d\Omega = 0 \quad (3.30)$$

$$\int_{\Omega^e} \left(\frac{h_s^2}{2} \frac{\partial W}{\partial y} \right) d\Omega + \int_{\Gamma^e} W \left(\frac{-h_s^2}{2} n_y \right) d\Gamma + \int_{\Omega^e} W \left(h_s \frac{\partial h_s}{\partial y} \right) d\Omega = 0 \quad (3.31)$$

For a non-flat and arbitrary bed topography, equations (3.30) and (3.31) are not satisfied in dry elements. In order to balance the discrete form of the momentum equations for all elements, a modified bottom topography $\tilde{h}_s = \{\tilde{h}_{s1}, \tilde{h}_{s2}\}$ can be computed for element e such that

$$\int_{\Omega^e} W \left(\tilde{h}_{s1} \frac{\partial h_s}{\partial x} \right) d\Omega = - \int_{\Omega^e} \left(\frac{h_s^2}{2} \frac{\partial W}{\partial x} \right) d\Omega + \int_{\Gamma^e} W \left(\frac{h_s^2}{2} n_x \right) d\Gamma \quad (3.32)$$

$$\int_{\Omega^e} W \left(\tilde{h}_{s2} \frac{\partial h_s}{\partial y} \right) d\Omega = - \int_{\Omega^e} \left(\frac{h_s^2}{2} \frac{\partial W}{\partial y} \right) d\Omega + \int_{\Gamma^e} W \left(\frac{h_s^2}{2} n_y \right) d\Gamma \quad (3.33)$$

Since $\tilde{h}_s^e = \sum_{k=1}^{npe} \tilde{h}_{s_k} \psi_k$, the nodal values of $\tilde{h}_s$ must be calculated through solving the momentum equations for all elements simultaneously. However, $\tilde{h}_{s1}$ and $\tilde{h}_{s2}$ for the x- and y-directions may be computed separately as the equations above are de-coupled. The resulting system has the following

form for each direction

$$[\mathbf{LHS}]_\xi \left\{\tilde{h}_s\right\}_\xi = [\mathbf{RHS}]_\xi \tag{3.34}$$

with

$$\begin{aligned}
\mathbf{LHS}_{i,j} &= \int_{\Omega^e} W_i \, W_j \left(\frac{\partial h_s}{\partial x_\xi}\right)_e d\Omega \\
\mathbf{RHS}_i &= -\int_{\Omega^e} \left(\frac{h_s^2}{2}\right)_e \frac{\partial W_i}{\partial x_\xi} \, d\Omega + \int_{\Gamma^e} W_i \left(\frac{h_s^2}{2}\right)_e n_{x_\xi} \, d\Gamma
\end{aligned} \tag{3.35}$$

where ξ represent the direction, i.e., $\xi = 1$ is for x-direction and $\xi = 2$ is for y-direction. The second term in $\mathbf{RHS}_i$ is evaluated for boundary edges only. The evaluation of nodal balancing $\left\{\tilde{h}_s\right\}_\xi$ is performed only once, and may be performed at the beginning of the solution procedure.

3.6.2 Partially-wet elements

In partially-wet elements, where water depth is zero at some nodes and is non-zero at others, the interpolated depth in the element will not represent the real water surface. Thus, further consideration is required to prevent a spurious water surface in partially-wet elements. Such elements can be included or excluded from the computations, however, both approaches result in an incorrect mass of water in the domain. By excluding partially-wet elements from the computations, an artificial barrier is assumed at the last wet node, as in Figure (3.2a), which changes the actual location of the shoreline and excludes some mass of water from the calculations. With including those elements within the numerical solution, a volume of air will be treated as mass of water as illustrated in Figure (3.2b). Since in the present study all types of elements are included in

the computational domain, spurious oscillations in wetting-drying fronts are unavoidable. For cases with arbitrary free surface elevations, the error may be reduced by using mesh refinement. However, for still-water conditions on non-flat bed, the water surface level can be accurately retrieved by applying modifications to the momentum equation. The x-momentum equation in (3.28) for still-water condition ($u = v = 0$) is given by

$$
\begin{aligned}
&-\int_{\Omega^e}\left(\frac{h^2}{2}\frac{\partial W}{\partial x}\right)d\Omega+\int_{\Omega^e}\left(\frac{h_s^2}{2}\frac{\partial W}{\partial x}\right)d\Omega+\int_{\Gamma^e}\left(W\frac{h^2}{2}\,n_x\right)d\Gamma\\
&-\int_{\Gamma^e}\left(W\frac{h_s^2}{2}\,n_x\right)d\Gamma-\int_{\Omega^e}\left(W\,h\,\frac{\partial h_s}{\partial x}\right)d\Omega+\int_{\Omega^e}\left(W\,h_s\,\frac{\partial h_s}{\partial x}\right)d\Omega=0
\end{aligned}
\tag{3.36}
$$

Introducing $\tilde{h}_s$, equation (3.36) may be rewritten as

$$
\begin{aligned}
&-\int_{\Omega^e}\left(\frac{h^2}{2}\frac{\partial W}{\partial x}\right)d\Omega+\int_{\Omega^e}\left(\frac{h_s^2}{2}\frac{\partial W}{\partial x}\right)d\Omega+\int_{\Gamma^e}\left(W\frac{h^2}{2}\,n_x\right)d\Gamma\\
&-\int_{\Gamma^e}\left(W\frac{h_s^2}{2}\,n_x\right)d\Gamma-\int_{\Omega^e}\left(W\,h\,\frac{\partial h_s}{\partial x}\right)d\Omega+\int_{\Omega^e}\left(W\,\tilde{h}_s\,\frac{\partial h_s}{\partial x}\right)d\Omega=0
\end{aligned}
\tag{3.37}
$$

By substituting equation (3.32) into equation (3.37), to meet the still-water condition for partially-wet elements will require

$$
\int_{\Omega^e}\left(W\,h\,\frac{\partial h_s}{\partial x}\right)d\Omega=-\int_{\Omega^e}\left(\frac{h^2}{2}\frac{\partial W}{\partial x}\right)d\Omega+\int_{\Gamma^e}\left(W\frac{h^2}{2}\,n_x\right)d\Gamma \tag{3.38}
$$

To satisfy the equality in equation (3.38), the only modification for partially-wet elements will be

$$
\frac{\partial h_s}{\partial x}=\frac{\partial h}{\partial x}\qquad or\qquad \frac{\partial \zeta}{\partial x}=0 \tag{3.39}
$$

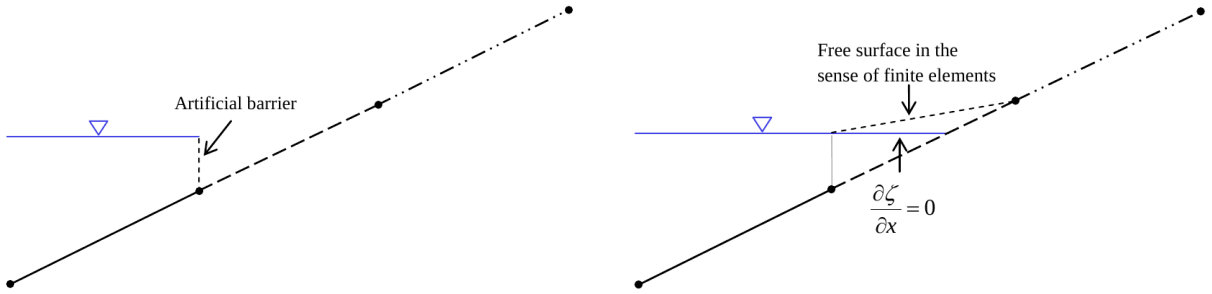

(a) Element exclusion approximation (b) Element inclusion approximation

Figure 3.2 Partially-wet elements treatment in fixed grid models

That is, the water surface gradient in the x-direction should be forced to zero at partially-wet elements in order to eliminate the spurious water surface. In a similar manner, since the momentum equations are decoupled, it can be shown that the water surface gradient in the y-direction should be forced to zero as well. Resulting in the condition

$$\frac{\partial h_s}{\partial y} = \frac{\partial h}{\partial y} \quad or \quad \frac{\partial \zeta}{\partial y} = 0 \tag{3.40}$$

CHAPTER 4

NUMERICAL RESULTS

This chapter presents the various test cases that have been used to validate the developed finite volume and finite element methodologies. The influence of arbitrary bed topography, dry regions, as well as advection and diffusion of contaminant are considered to examine the stability and robustness of the present schemes. Dam-break test cases are simulated to highlight the shock-capturing feature in wet or dry regions with arbitrary bed topography. The pollution transport test cases are presented to demonstrate advection and diffusion of contaminant within the flow.

4.1 Finite Volume Results

In order to verify the current finite volume method (FVM), several test cases are considered. Wet and dry dam break problems, oscillation of a bead of water in a parabolically-shaped bowl, and supercritical flow in a constricted channel are simulated to verify performance of the current algorithm with zero contaminant. Other test cases are discussed to verify advection and diffusion of contaminant with the flow. The simulation of contaminant transport in a notional river is also simulated to demonstrate that the present work can be implemented on practical applications involving flooding and pollutant transport.

4.1.1 Dam-Break

Dam-break problems are traditional test cases for shallow water models. In the current work, this test case consists of a nondimensional region spanning from 0.0 to 1.0, having uniform, but dissimilar left and right water levels separated by a wall located at $x = 0.5$, as shown in Figure (4.1). The wall is removed at $t = 0$, which produces a left-running rarefaction wave and a right-running discontinuous shock wave. Exact solutions for this Riemann problem are given in Toro [11] for both *wet-bed* and *dry-bed* scenarios. A two-dimensional grid is used, with a streamwise mesh spacing of $\Delta s = 0.0025$, and the computed heights and velocities along the horizontal centerline of the domain are compared to the exact solutions. No bottom friction is imposed for dam-break cases.

Initially, a *wet-bed* dam-break problem is considered with the water level 1.0 and 0.05 for the left and right states, respectively ($h_L = 1.0, h_R = 0.05$). The initial discontinuity at $x = 0.5$ should move to the location $x = 0.75$ at time $t = 0.2366$. As shown in Figure (4.2), the current finite volume scheme predicts height and velocity accurately for both rarefaction and shock waves. Small overshoots are visible which are typical of upwind schemes.

A *dry-bed* dam-break problem with moving wet/dry interface is also considered. A water level of 1.0 on the left and a dry-bed on the right ($h_L = 1.0, h_R = 0.0$) is the initial condition for this test case. Many solution techniques are not capable of simulating this particular problem, as the system of equations has a singular point at $h = 0$. As shown in Figure (4.3), although the water depths are accurately captured, the horizontal velocity is sensitive to the choice of ϵ. Recall, this parameter is responsible for masking the singularity in the inverse of the transformation matrix.

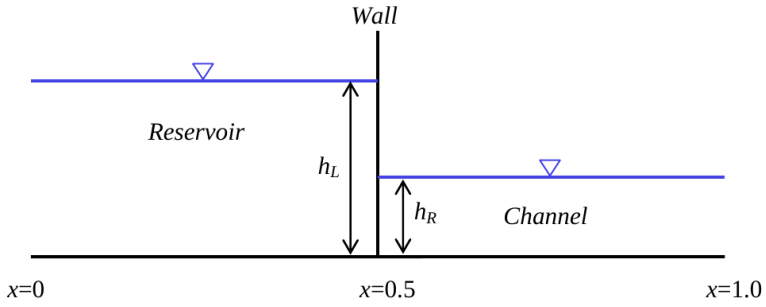

Figure 4.1 The traditional dam-break problem

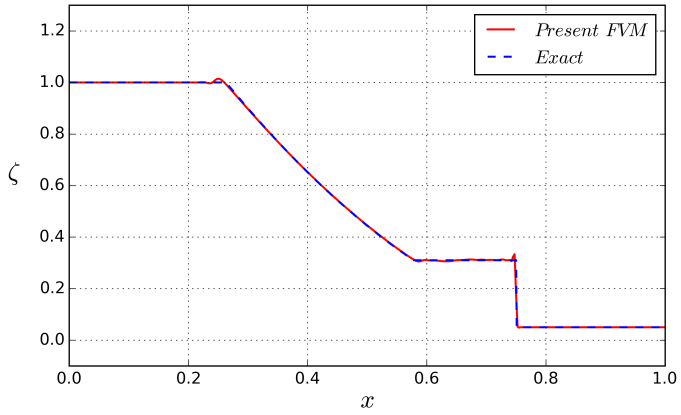

(a) Water Surface, $\Delta s = 0.0025$.

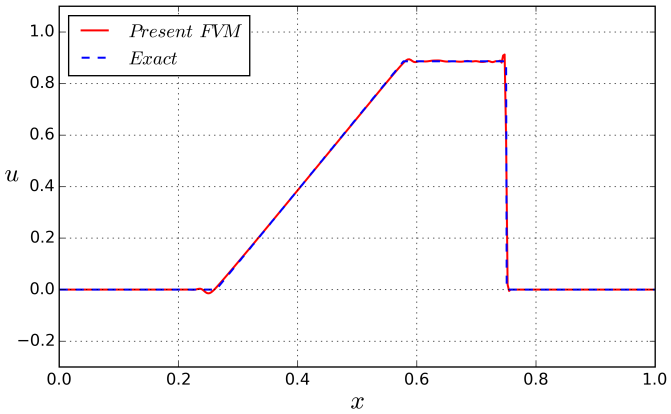

(b) Horizontal Velocity, $\Delta s = 0.0025$.

Figure 4.2 Numerical and theoretical solutions for the wet-bed dam-break problem at t = 0.2366

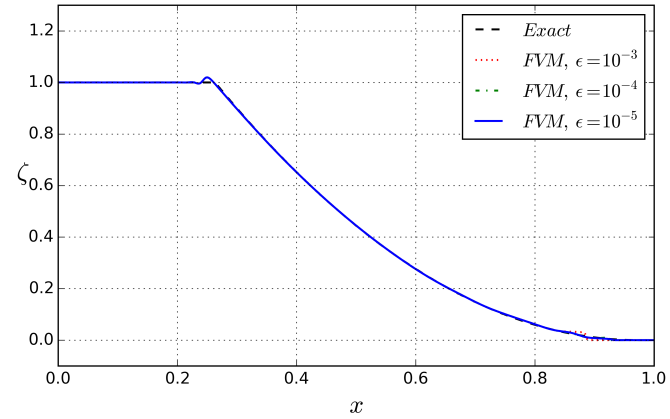

(a) Water Surface, $\Delta s = 0.0025$.

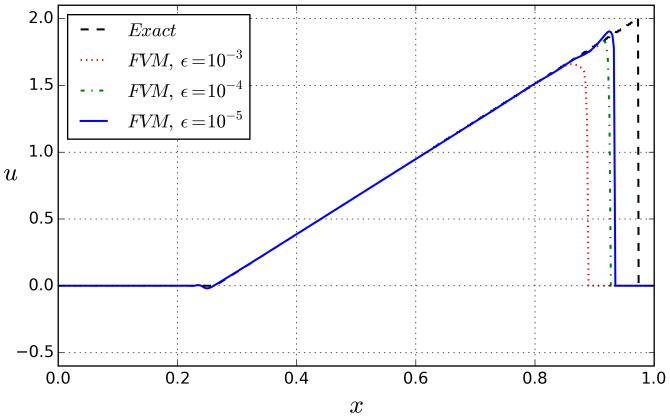

(b) Horizontal Velocity, $\Delta s = 0.0025$.

Figure 4.3 Numerical and theoretical solutions for the dry-bed dam-break problem at t = 0.2366

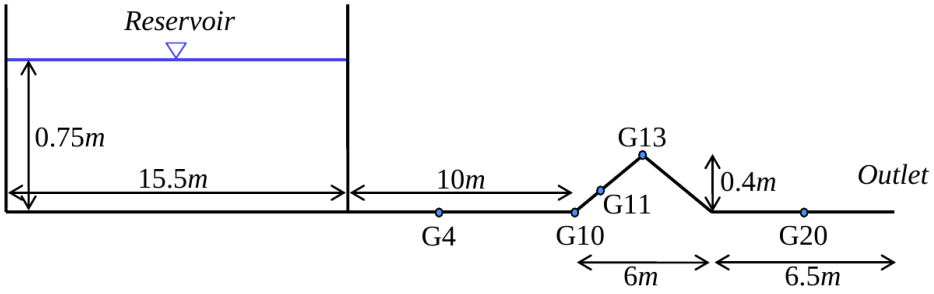

Figure 4.4 Geometry and gauge locations for the triangular obstacle case

4.1.2 Dam Break over a Triangular Obstacle

This test case simulates the evolution of a dam break wave over a triangular obstacle. The experimental data was obtained at the Recherches Hydrauliques Lab Chatelet in coordination with the Université libre de Bruxelles (Belgium) [60]. As illustrated in Figure (4.4), the model consists of a reservoir and a channel separated by a dam, and a triangular obstacle downstream of the dam. The slopes of triangular obstacle are symmetric. At $t = 0$, the water level is $0.75\,m$ in the reservoir and zero in the rest of the channel (dry bed). All boundaries are considered as walls except for the free outlet, and the Manning roughness coefficient is $n = 0.0125\,s.m^{-1/3}$. The computational domain for this test case is a two-dimensional rectangular channel discretized with a uniform unstructured grid. To validate the accuracy of the numerical scheme, experimental and numerical results are compared at the measurement locations. Table (4.1) and Figure (4.4) display the location of each gauge. Figure (4.5) presents the numerical and experimental water depth (h) as a function of time at the various gauge locations. Additionally included in this Figure are the finite volume numerical results from Brufau [60]. A direct comparison of the present results with Brufau [60] is shown in Figure (4.6). In this Figure the water depth along the spatial domain at various time snapshots may be observed. The results presented demonstrate excellent agreement with both experimental data and with Brufau [60].

Table 4.1 Gauge locations for the triangular obstacle case

Gauge number	$x(m)$	$y(m)$
G4	19.5	0.0
G10	25.5	0.0
G11	26.5	0.0
G13	28.5	0.0
G20	35.5	0.0

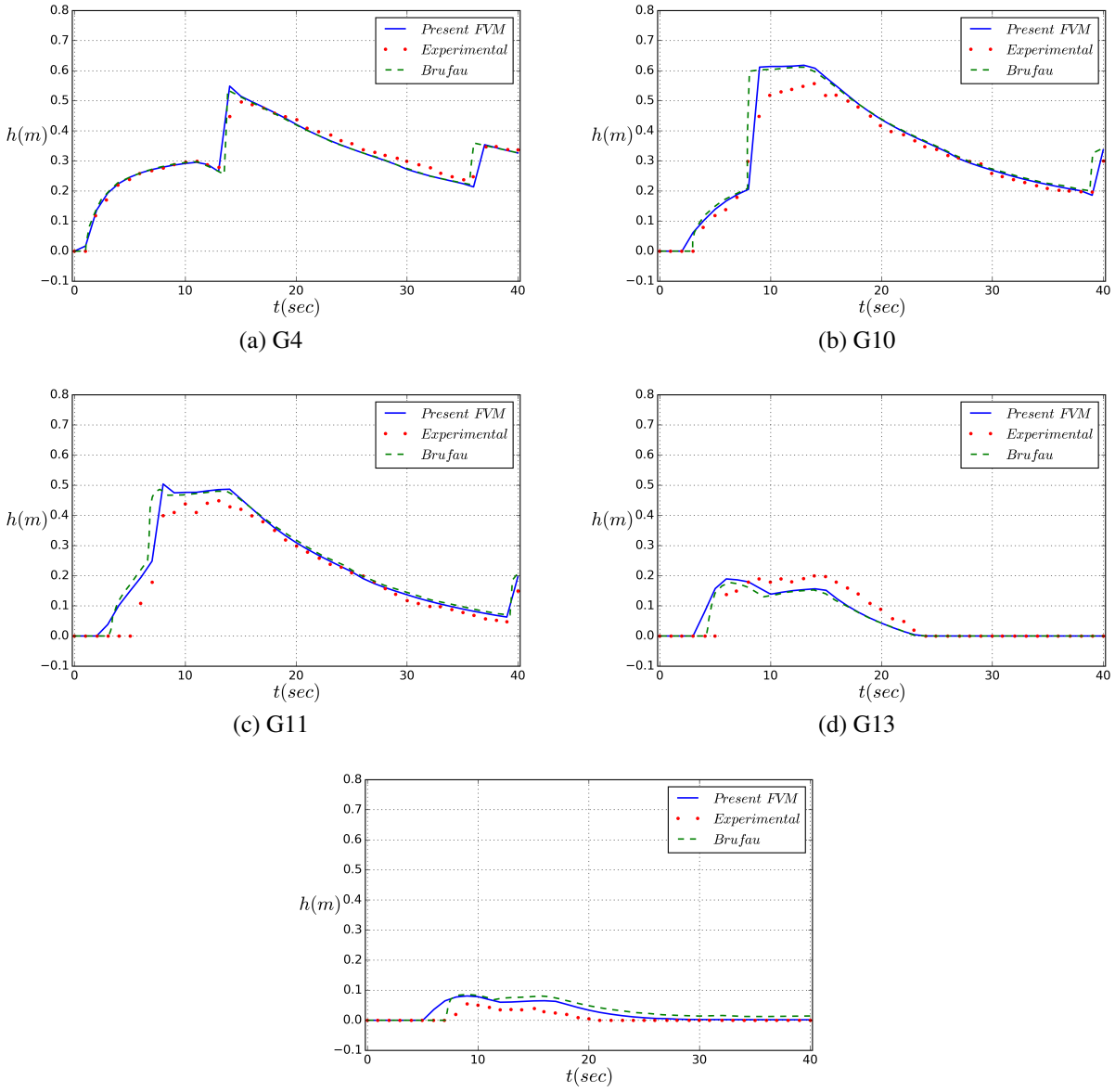

(a) G4

(b) G10

(c) G11

(d) G13

(e) G20

Figure 4.5 Measured and computed water depth at gauge locations for the triangular obstacle case

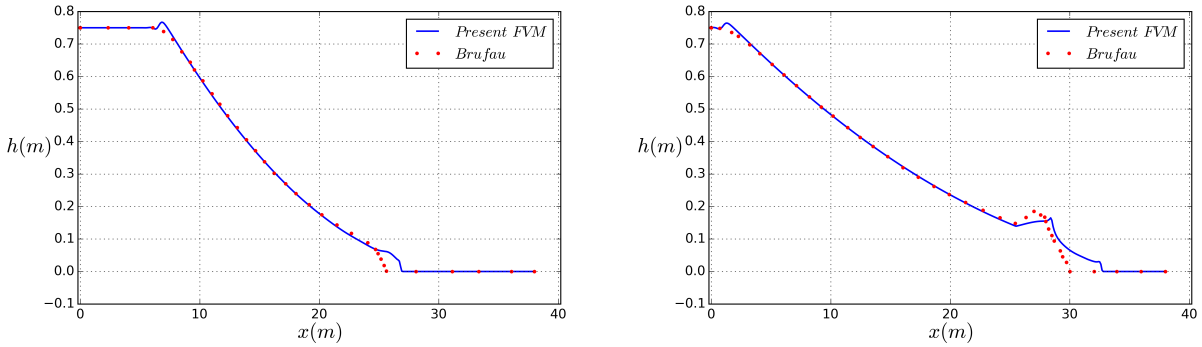

(a) t=3 sec

(b) t=5 sec

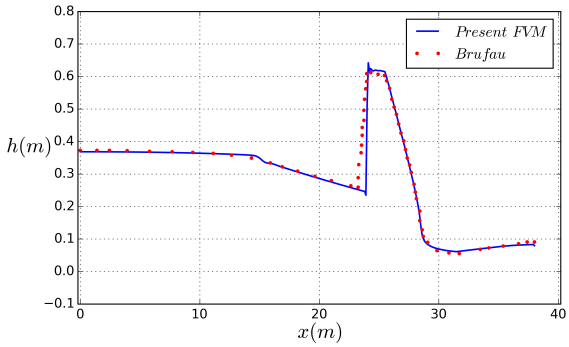

(c) t=10 sec

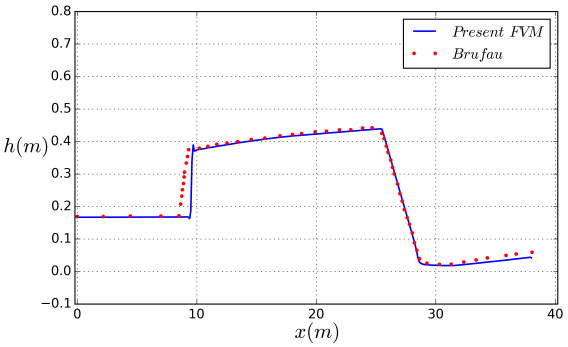

(d) t=20 sec

Figure 4.6 Computed water depth profile in different times for the triangular obstacle case

4.1.3 Parabolic Basin

In order to highlight the stability and robustness of the present FVM in accommodating wetting-drying fronts on a non-flat bed, oscillations of a bead of water in a parabolically-shaped basin is considered. This test problem and an analytical solution are given in [61]. In this case, there is no bottom friction inside the basin and all boundaries have the Dirichlet condition. The exact solution for the free-surface elevation is given by

$$\zeta = h - h_s = \frac{\sqrt{1 - A^2}}{1 - A\,\cos(\omega t)} - \frac{r^2}{a^2}\left(\frac{1 - A^2}{(1 - A\,\cos(\omega t))^2} - 1\right) - 1 \tag{4.1}$$

where t is the elapsed time, $r = \sqrt{x^2 + y^2}$, $A = \frac{a^4 - r_0^4}{a^4 + r_0^4}$ and $\omega = \sqrt{8}/a$. The still-water surface elevation, defined by $\zeta = 0$, has unit depth at the centerline $r = 0$ with a circular *shoreline* located at $r = a$. The computational domain shown in Figure (4.7) is a square ranging from -1.0 to 1.0 in both x- and y- directions and an isotropic unstructured mesh is used to discretize the domain. As shown in Figure (4.8), the water level is initialized with the exact solution at $t = 0$, which intersects the bottom at $r = r_0$. In this study, $a = 0.75$, $r_0 = 0.60$ and the bottom topography of the parabolic bowl is defined by $h_s = 1 - r^2/a^2$. Furthermore, the period of oscillation is given as $T = 2\pi/\omega \approx 166.608$.

As shown in Figures (4.9) and (4.10), the computed solution is indistinguishable from the theoretical solution. Figure (4.9) depicts the surface elevation at the center of the parabolic basin as a function of period. Even after 10 periods have elapsed, excellent agreement with the analytical solution is observed. Figures (4.10a) and (4.10c) illustrate the surface elevation across the center

line of the parabolic basin at time $10T$ and $11.3T$, respectively. In these Figures, the wetting-drying fronts can be clearly seen. Furthermore, Figures (4.10b) and (4.10d) show the water depth contours on the two-dimensional mesh at the aforementioned times.

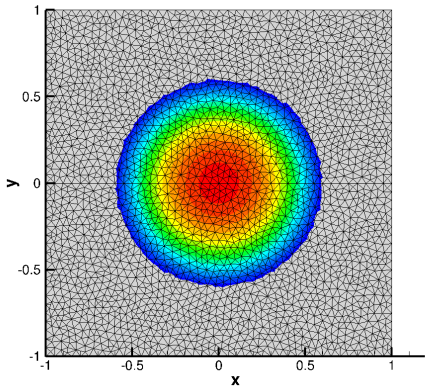

Figure 4.7 The computational domain and initial water surface contours for the oscillating parabolic basin case

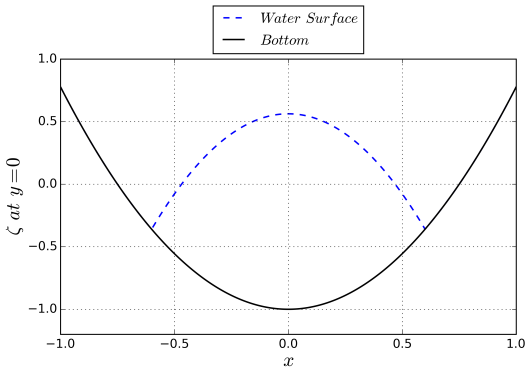

Figure 4.8 The initial solution for the oscillating parabolic basin case

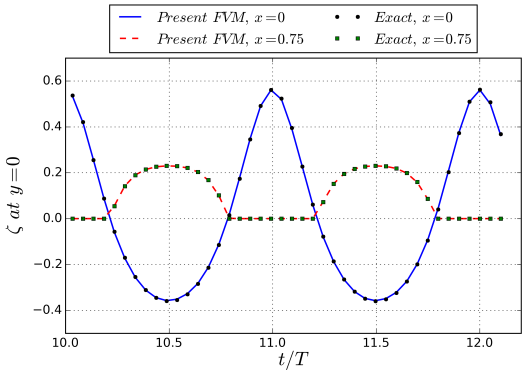

Figure 4.9 Water surface oscillation in the parabolic basin at selected points

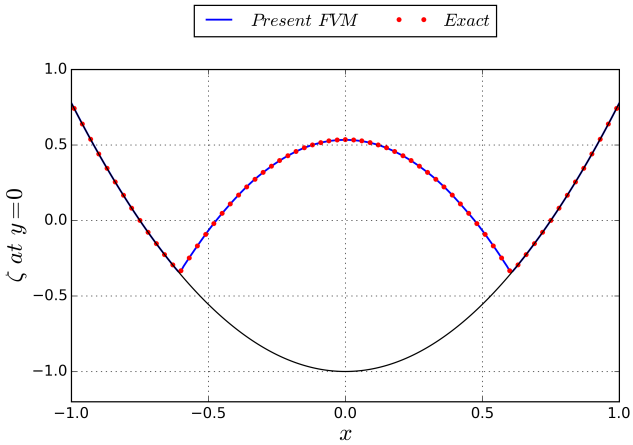

(a) Water surface at $t = 10T$.

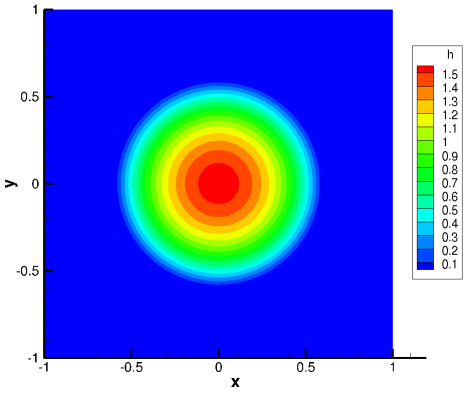

(b) Water depth contours at $t = 10T$.

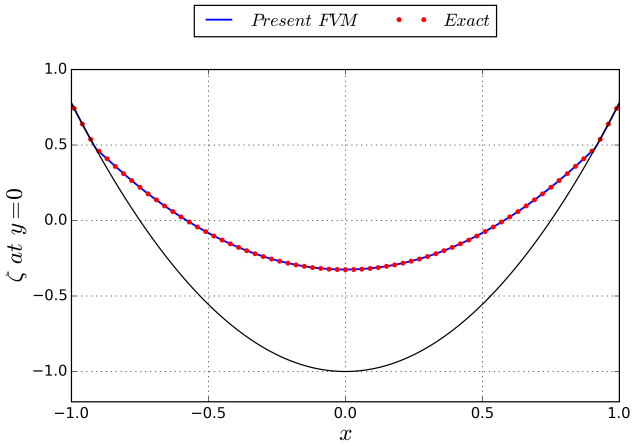

(c) Water surface at $t = 11.3T$.

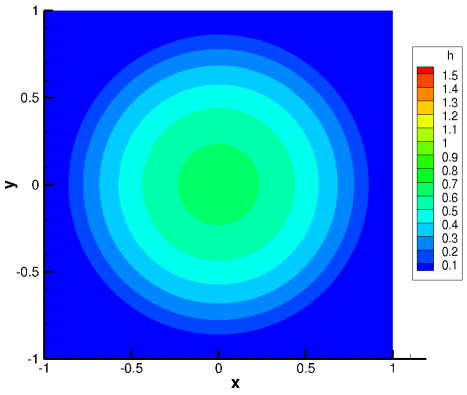

(d) Water depth contours at $t = 11.3T$.

Figure 4.10 Numerical and theoretical solutions of water depth in the parabolic basin

4.1.4 Supercritical Flow in a Constricted Channel

The steady state flow in a constricted channel, with a Froude number of 4.0, is considered to demonstrate performance of the current FVM in simulating supercritical flows. This test case was previously considered experimentally [62] and computationally [63, 64]. The problem domain is a 0.61 m wide channel transitioning to a 0.3 m wide channel at a convergence angle of 6°. The two-dimensional unstructured mesh used for this simulation is shown in Figure (4.11a). Friction stresses and variation in bed slope are neglected in the present computations. For this supercritical flow, an oblique hydraulic jump is formed due to the change in cross-section. An effective numerical scheme should be capable of capturing these discontinuities.

Figure (4.11b) displays the water depth contours in the channel as well as the shock angle. The inclined walls produce an attached wave at an angle of 19.9° relative to the incoming flow direction which compares well with the analytical results of 19.68° presented in Figure (4.11c) [64].

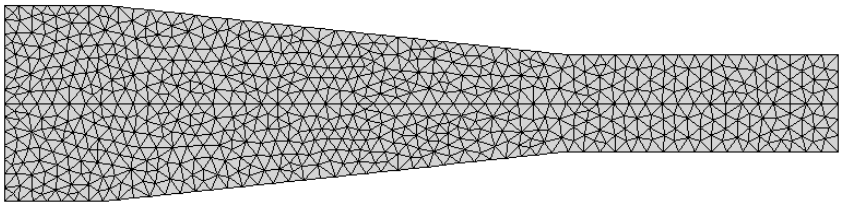

(a) Unstructured mesh (31543 triangular elements).

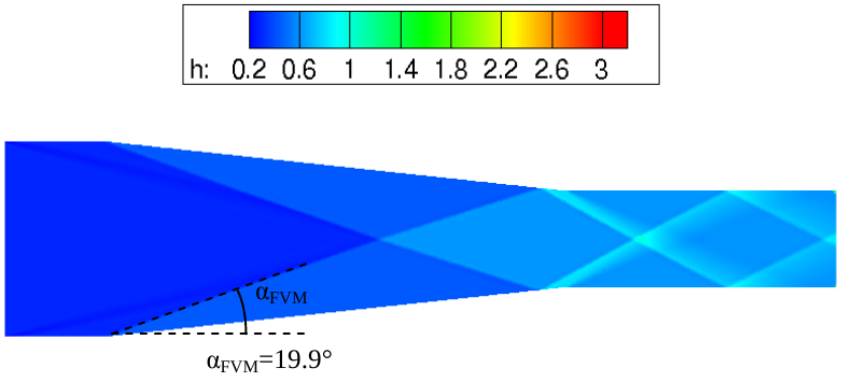

(b) Computed water depth contours.

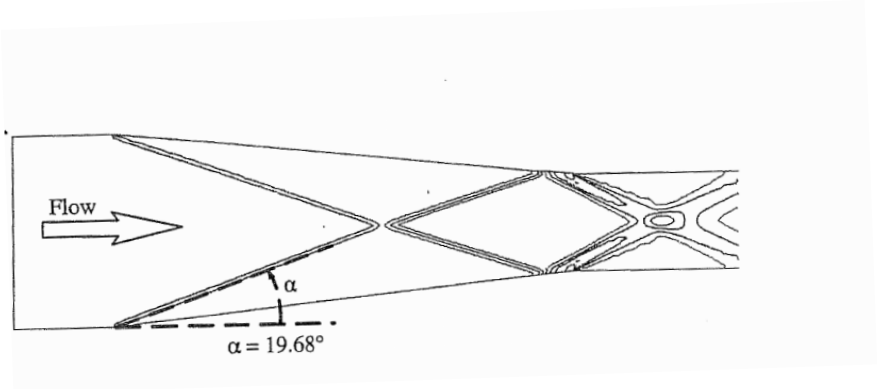

(c) Analytical results.

Figure 4.11 Supercritical flow in a constricted channel

4.1.5 Pollutant Advection

The test problem from [3] is considered to demonstrate the ability of the present FVM in simulating contaminant transport. This test case is described as pure advection of a contaminant in a square domain. In the present work, the topology is assumed to be smooth and flat and there are no frictional forces. The computational domain is a $9km \times 9km$ square channel, which is discretized with a nonuniform unstructured grid. A uniform flow with $u = v = 0.5\,m/s$ and $h = 0.2485\,m$ is imposed on the entire domain. The initial pollutant concentration is defined by the superposition of two Gaussian distributions centered at $x_1 = y_1 = 1400\,m$ and $x_2 = y_2 = 2400\,m$, and is given as

$$\phi = \phi_1\, e^{-\frac{{d_1}^2}{{\sigma_1}^2}} + \phi_2\, e^{-\frac{{d_2}^2}{{\sigma_2}^2}} \tag{4.2}$$

$$d_1 = \sqrt{(x - x_1)^2 + (y - y_1)^2} \tag{4.3}$$

$$d_2 = \sqrt{(x - x_2)^2 + (y - y_2)^2} \tag{4.4}$$

The above constants are chosen to be

$$\phi_1 = 10 \qquad \phi_2 = 6.5 \qquad \sigma_1 = \sigma_2 = 264 \tag{4.5}$$

Inflow and outflow conditions are applied appropriately on the boundaries. The exact solution consists of the pollutant concentration moving diagonally across the domain with the constant speed of $u = v = 0.5\,m/s$ while retaining the initial distribution shape. Figure (4.12) illustrates the computed results compared to the theoretical solution at different times.

4.1.6 Pollutant Diffusion

The diffusion of a Gaussian distribution of contaminant in still water is considered here to examine the accuracy of the current FVM in numerically simulating the diffusion of pollutant. A square domain ranging from -2.0 to 2.0 with a flat and smooth bottom is assumed as the computational domain. Considering a constant water depth of $h = 0.01$ at rest, the velocity components are zero. The initial distribution of contaminant is a Gaussian distribution centered at $x_0 = y_0 = 0.0$ with the maximum value of 1.0 and standard deviation of $\sigma = 0.1$ and is given by

$$\phi(x, y, 0) = e^{-\frac{(x-x_0)^2+(y-y_0)^2}{\sigma^2}} \tag{4.6}$$

The analytical solution for this problem given in [65] may be expressed as

$$\phi(x, y, t) = \frac{\sigma^2}{4\,D\,t + \sigma^2}\, e^{[-\frac{(x-x_0)^2}{4\,D\,t+\sigma^2} - \frac{(y-y_0)^2}{4\,D\,t+\sigma^2}]} \tag{4.7}$$

where the diffusion coefficient in all directions is $D = 0.01$. Computations are carried out on a uniform unstructured grid with $\Delta x = \Delta y = 0.02$, and integrated over the nondimensional time interval [0,15]. Shown in Figure (4.13) are the numerical and theoretical contaminant distributions at various time snapshots. Figures (4.13b), (4.13d) and (4.13f) illustrate the contaminant contours on the two-dimensional mesh. Furthermore, Figure (4.14) depicts the numerical and analytical rates of diffusion of the contaminant at two points within the domain. As can be observed for this validation case, excellent agreement is obtained.

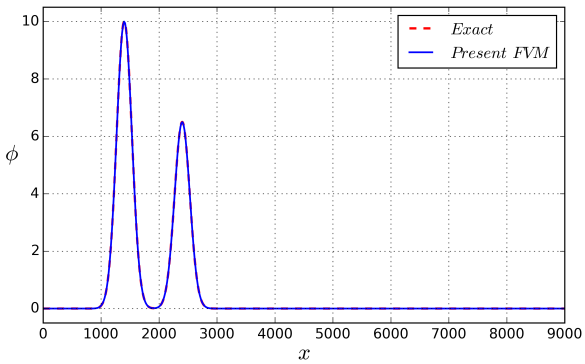

(a) Contaminant distribution at $t = 0$.

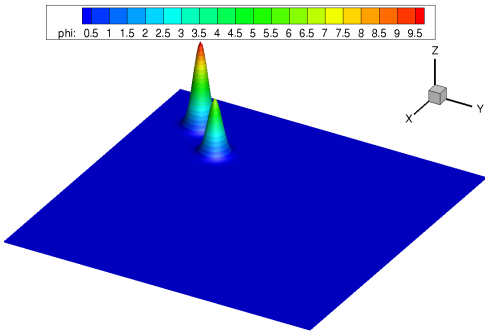

(b) Contaminant contours at $t = 0$.

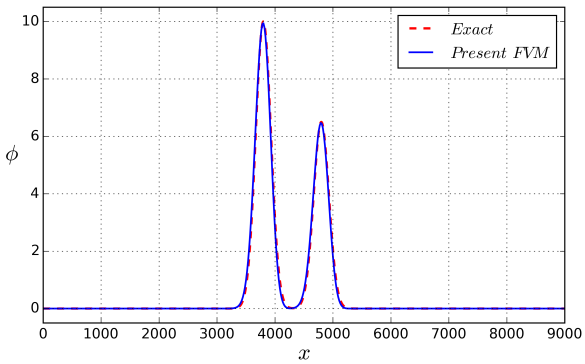

(c) Contaminant distribution at $t = 4800$ sec.

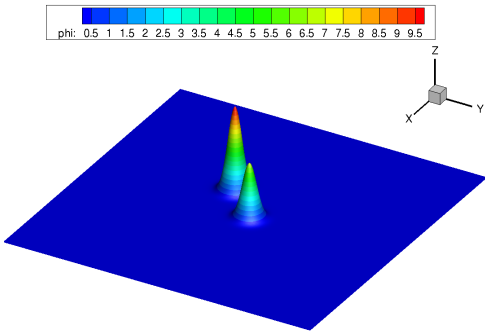

(d) Contaminant contours at $t = 4800$ sec.

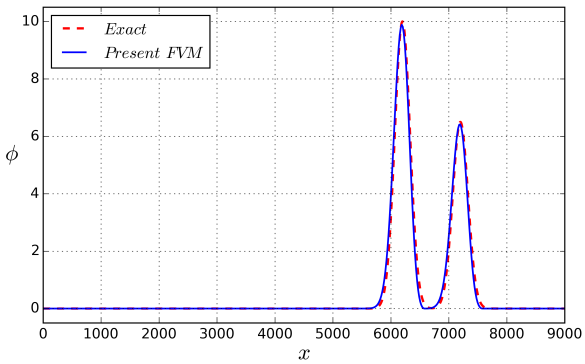

(e) Contaminant distribution at $t = 9600$ sec.

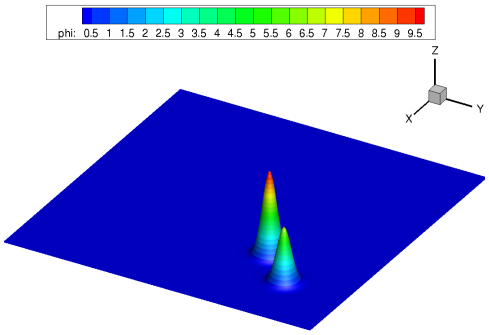

(f) Contaminant contours at $t = 9600$ sec.

Figure 4.12 Contaminant distribution in the square cavity test case

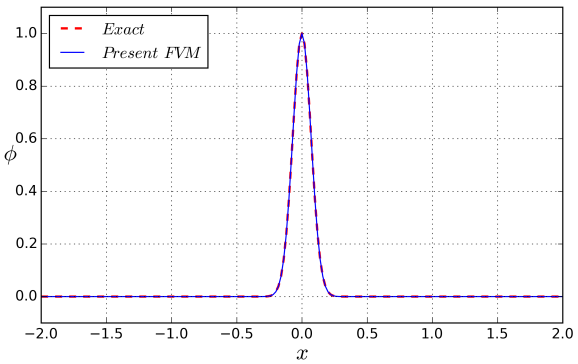

(a) Contaminant distribution at $t = 0$.

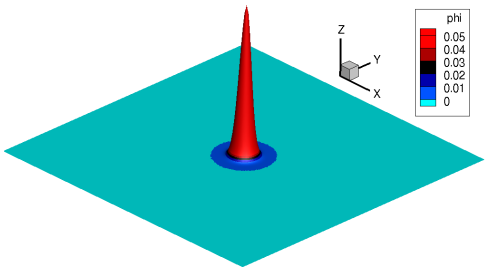

(b) Contaminant contours at $t = 0$.

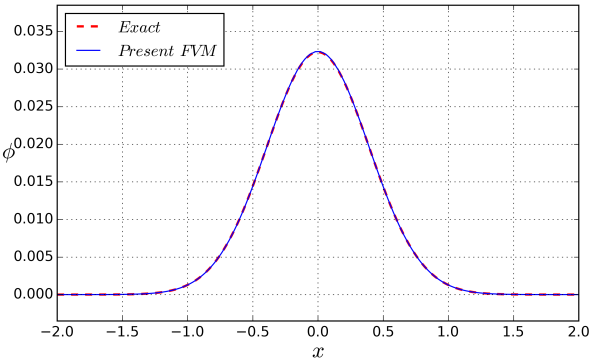

(c) Contaminant distribution at $t = 7.5$.

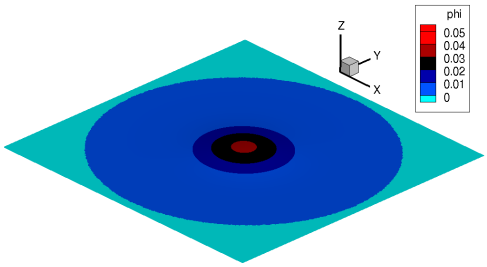

(d) Contaminant contours at $t = 7.5$.

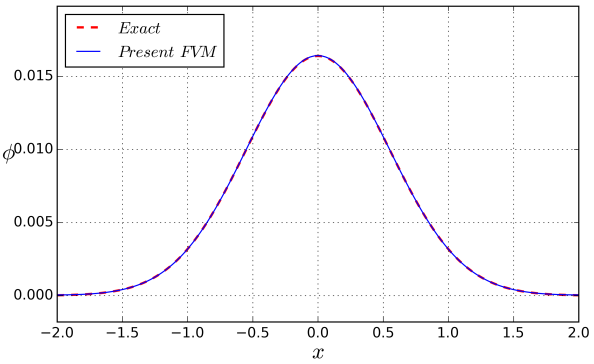

(e) Contaminant distribution at $t = 15$.

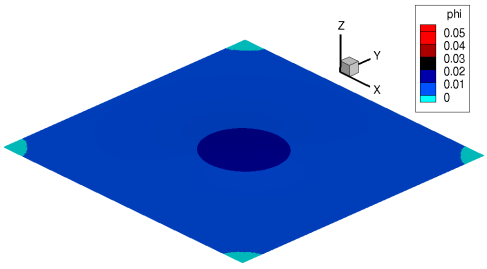

(f) Contaminant contours at $t = 15$.

Figure 4.13 Contaminant distribution in different times for the pollutant diffusion test case

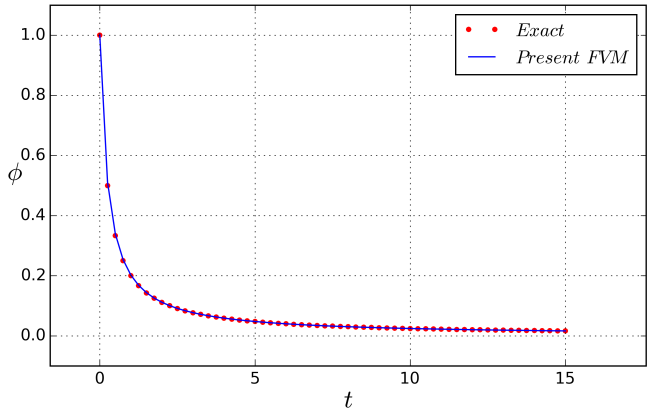

(a) $x = 0,\ y = 0$

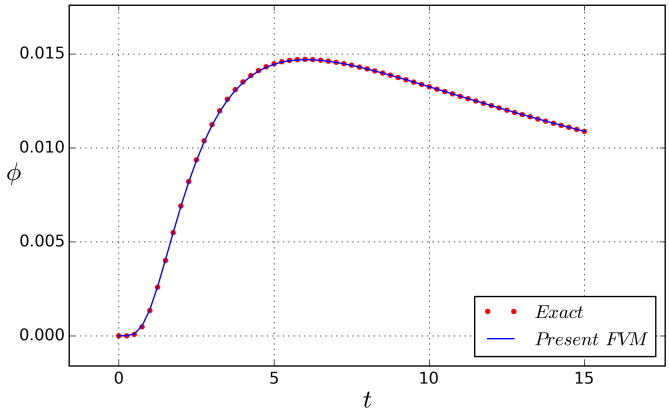

(b) $x = 0.5,\ y = 0$

Figure 4.14 Contaminant level in selected points for the pollutant diffusion test case

4.1.7 Pollutant Transport in a Notional River following a Flood

A scaled river model is designed to demonstrate the ability of the present FVM for real-world problems and to simulate contaminant transport over complex and irregular topography. As shown in Figure (4.15), the river geometry consists of three inlets, two outlets, seven islands, and the bathymetry varies within the domain. The computational domain is decomposed into 183524 triangular elements and the wall boundary condition is imposed on the land and island boundaries. The river is initially at steady state with pollutant source located at (0.495,0.535), having a radius of 0.005, and a nondimensional concentration of 20. The Manning roughness coefficient is assumed to be $n = 0.0155$. At $t = 0$, a flood wave is released from inlet 1 and flows through the river and spreads the contaminant through the river system. As shown in Figure (4.15) and Table (4.2), several gauge stations are placed to record the flow variables at different times within the time interval of $t = [0, 1.5]$. The contours in Figure (4.15) illustrate the bottom topography.

Figure (4.16) displays the predicted water surface level and velocity components created by the flood wave at the gauge locations. The flow is originally at a steady state prior to the arrival of the flood wave. As seen, an abrupt change occurs in the water surface and velocity components once the flood wave reaches the gauge points, where the water surface rises and oscillates. Since in this case the flood wave is continuously applied at inlet 1 during the simulated time, the flow approaches a steady state as is evident from results at the gauges. Velocity components respond differently at the gauge locations due to the bathymetry of the river around those points. At gauges 1 to 3, velocity components approach a steady state more quickly. However, at gauge 4, which is located in a wide region connecting the flooded area by a narrow canal, more time is required for the velocity components to reach a steady state.

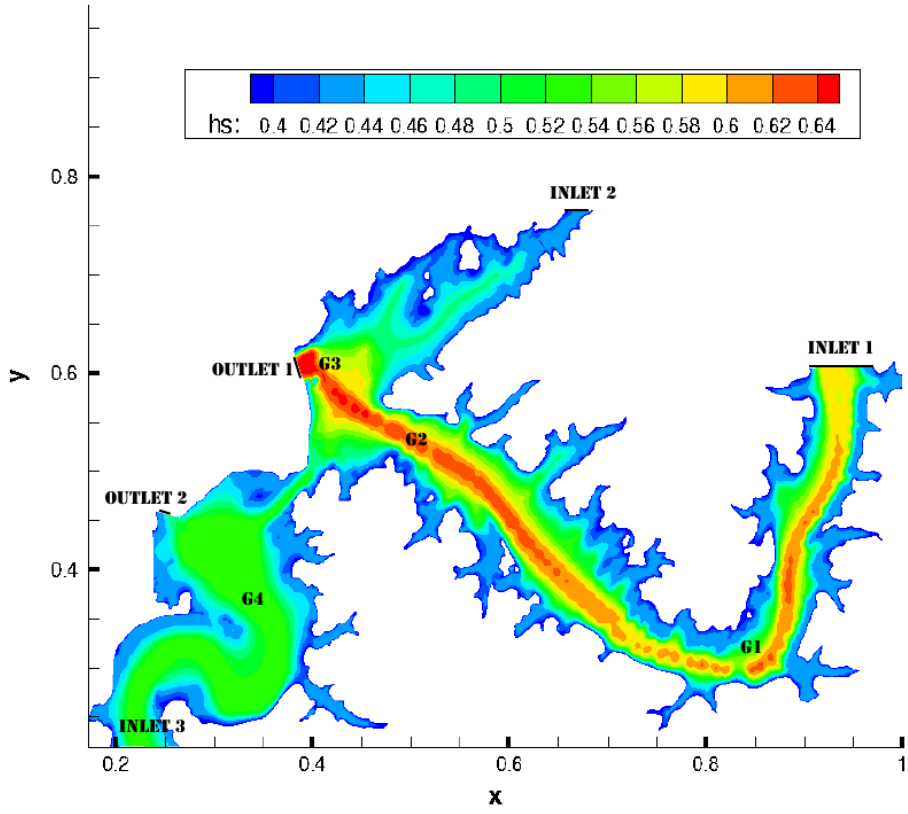

Figure 4.15 The notional river geometry, bottom topography contours and gauge locations

Figures (4.17) to (4.19) illustrate the spatial distribution of water surface and contaminant over the entire domain at distinct computational times. A comparison between the polluted area before and after the flood indicates that, depending on the flow depth and velocity, the pollution can contaminate many remote locations in the river system. This may be readily seen in Figures (4.18b), (4.18d) and (4.18f), that as the contaminant approaches outlet 1, which is not capable of evacuating the entire pollutant, large amounts enter the small channel towards gauge 4 as well as travel upwards towards inlet 2. Finally, as seen in Figure (4.18f) at $t = 1.5$, high concentrations of the pollutant remain trapped in the vicinity of the islands directly below inlet 2.

Table 4.2 Gauge locations for the notional river case

Gauge number	$x(m)$	$y(m)$
G1	8.533e-01	3.304e-01
G2	5.012e-01	5.620e-01
G3	4.012e-01	6.354e-01
G4	3.474e-01	3.537e-01

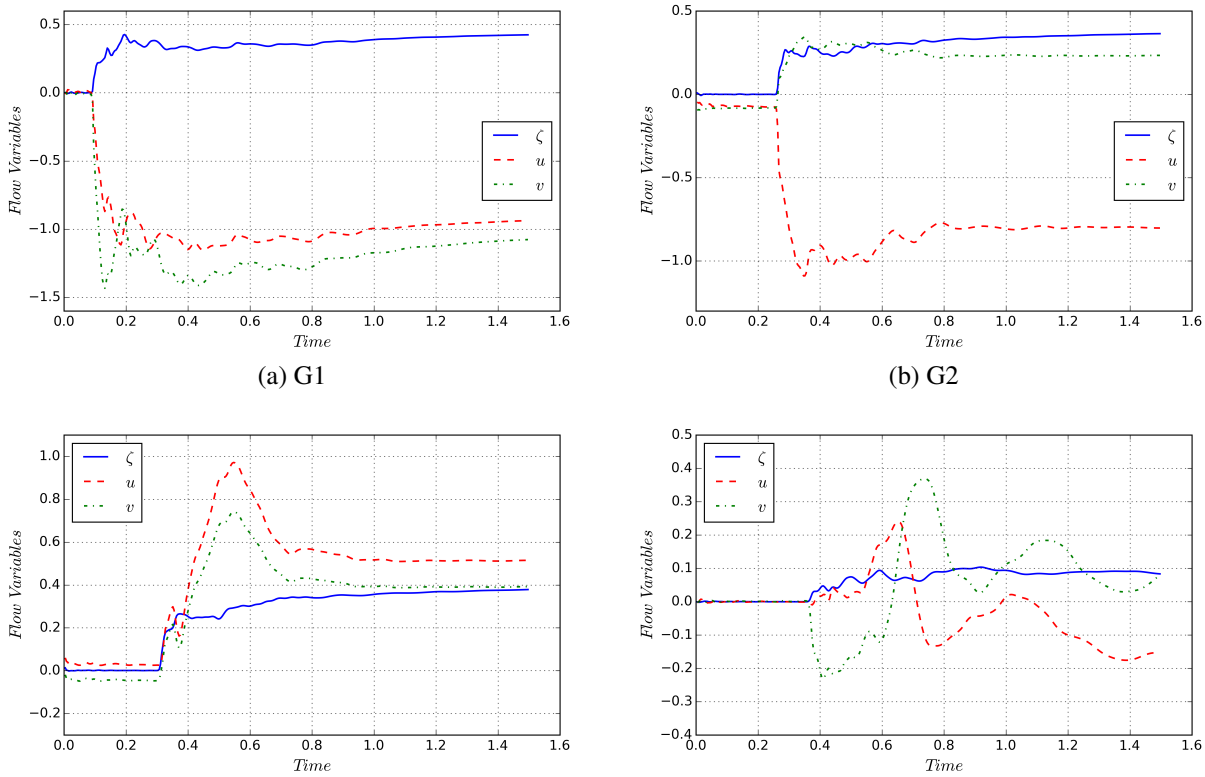

(a) G1 (b) G2

(c) G3 (d) G4

Figure 4.16 Water surface and velocity in different locations for the notional river case

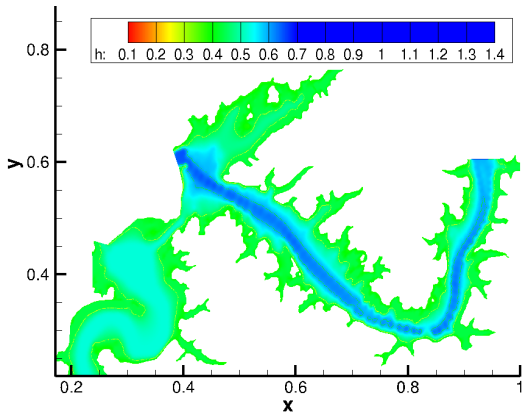

(a) Water depth at $t = 0$.

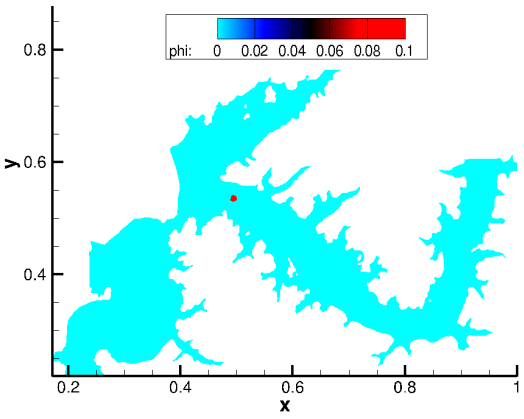

(b) Pollutant distribution at $t = 0$.

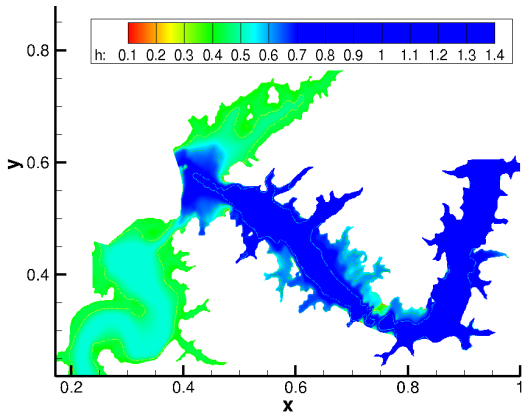

(c) Water depth at $t = 0.31$.

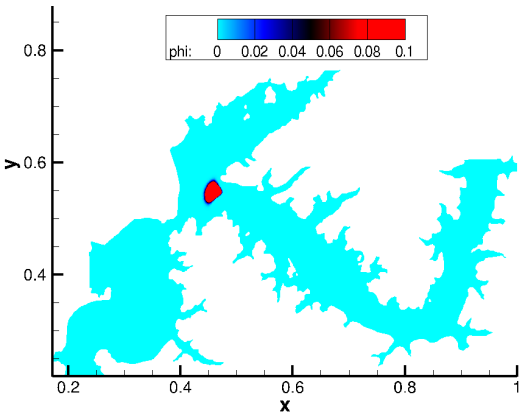

(d) Pollutant distribution at $t = 0.31$.

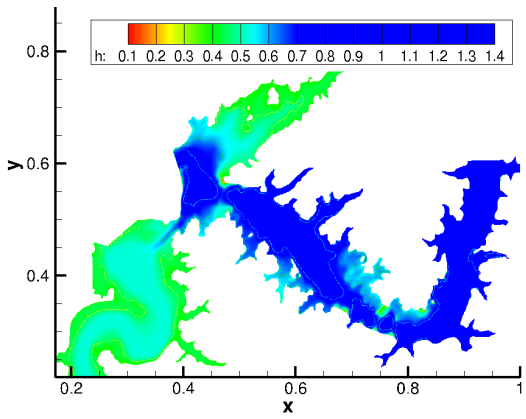

(e) Water depth at $t = 0.34$.

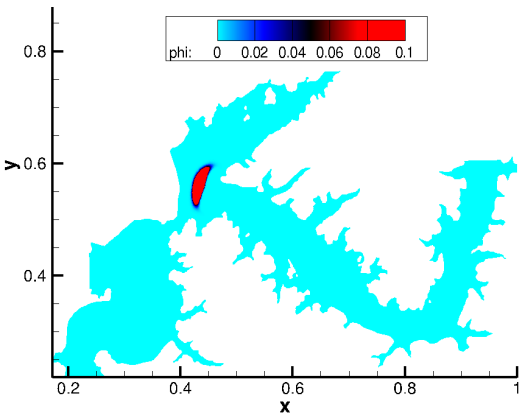

(f) Pollutant distribution at $t = 0.34$.

Figure 4.17 Distribution of water depth and contaminant for the notional river case

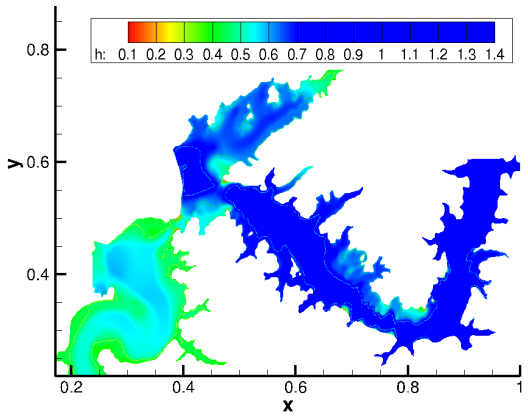

(a) Water depth at $t = 0.41$.

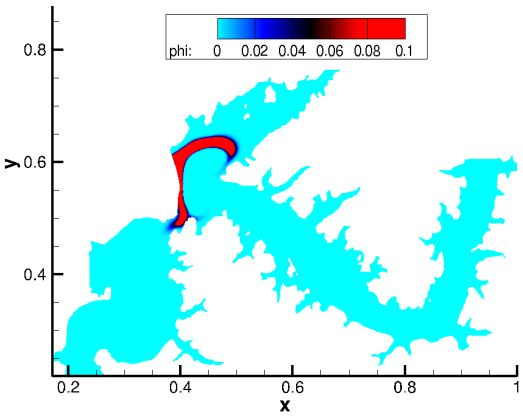

(b) Pollutant distribution at $t = 0.41$.

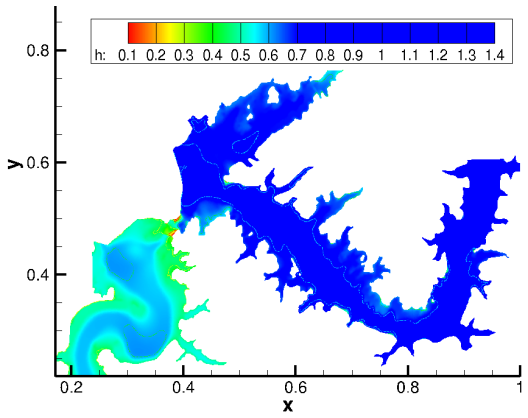

(c) Water depth at $t = 0.53$.

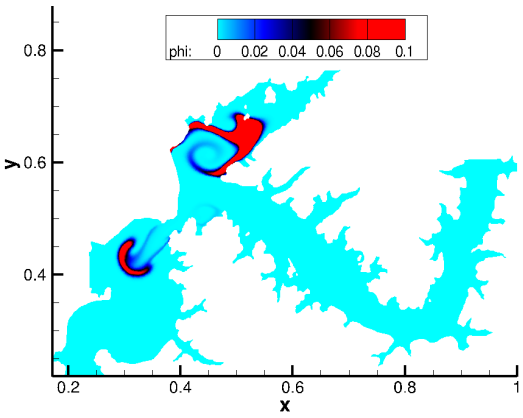

(d) Pollutant distribution at $t = 0.53$.

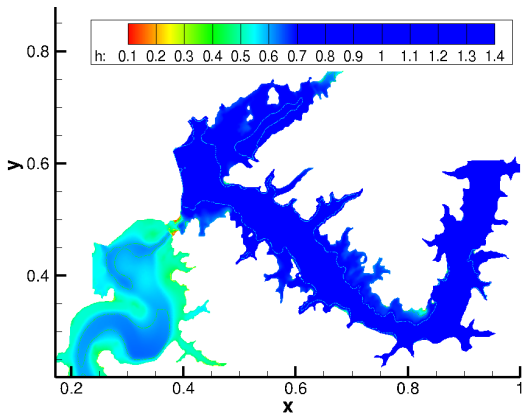

(e) Water depth at $t = 0.64$.

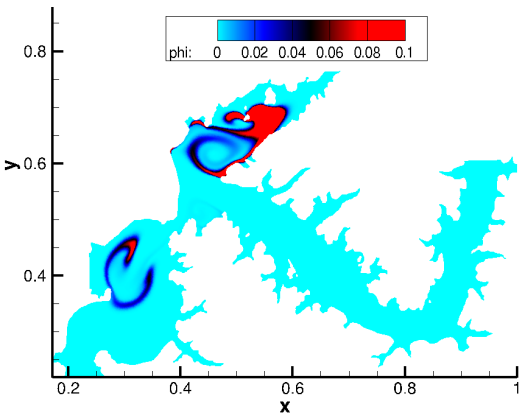

(f) Pollutant distribution at $t = 0.64$.

Figure 4.18 Distribution of water depth and contaminant for the notional river case

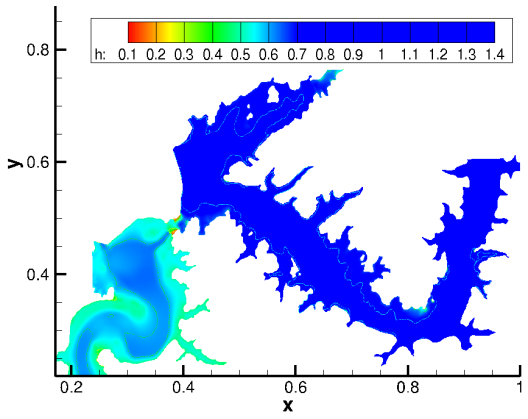

(a) Water depth at $t = 0.8$.

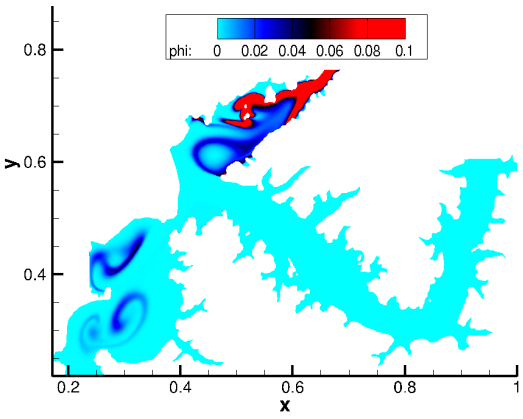

(b) Pollutant distribution at $t = 0.8$.

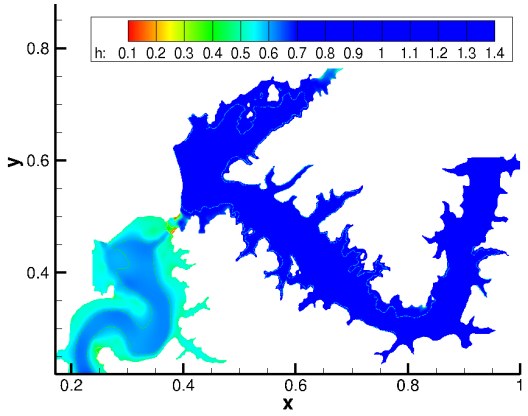

(c) Water depth at $t = 1.0$.

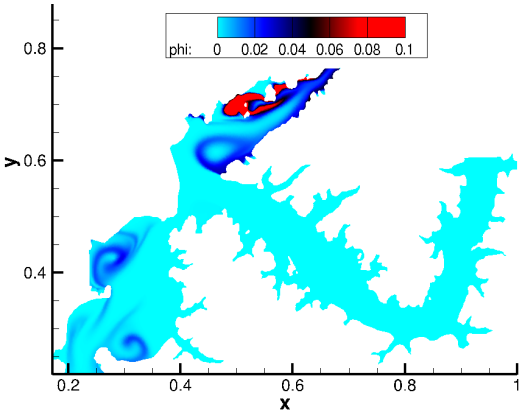

(d) Pollutant distribution at $t = 1.0$.

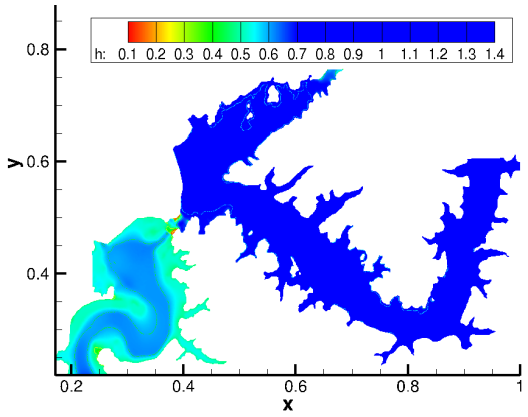

(e) Water depth at $t = 1.5$.

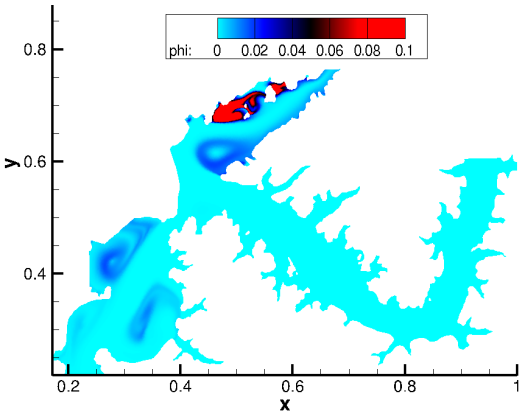

(f) Pollutant distribution at $t = 1.5$.

Figure 4.19 Distribution of water depth and contaminant for the notional river case

4.2 Finite Element Results

In this section, computational results of the developed finite element method are presented. For validation and verification, these results are compared to those obtained from analytical solutions and with the previously discussed finite volume method. All test cases utilize the same computational mesh, the same time step, and the same initial and boundary conditions in the simulations.

4.2.1 Dam-Break

The dry-bed and wet-bed dam break problems previously introduced are solved using the current FEM and compared to the present FVM and theoretical solutions. For this test case, the time step is selected as $\Delta t = 0.0001$. At nondimensional time t=0.2366 the water surface elevation and horizontal velocity are shown with two mesh resolutions in Figure (4.20) for the wet-dam break. The FEM stabilization parameter δ_{s1} more accurately predicts the location of the shock front as the mesh is refined, however, the overshoots around the discontinuity become more pronounce. The FEM stabilization parameter δ_{s2} appears to suppress these oscillations, however the horizontal velocity is over-predicted as the discontinuity is approached. Furthermore, this over-prediction becomes more evident on the finer grid.

Figure (4.21) depicts the results for the dry-dam break test case at the same time instant as was shown for the wet-dam break, but only for the finer mesh resolution using the stabilization parameter δ_{s1}. This figure shows the water surface elevation and horizontal velocity for two different values of ϵ. Recall, ϵ is the parameter used to avoid the singularity at zero water elevation. In terms of the water surface elevation, the FEM and FVM produce comparable results that are relatively

insensitive to the selected value of parameter ϵ. However, this is not the case for the horizontal velocity. As seen, as the value of ϵ becomes smaller, more accurate results are obtained. Moreover, from the profiles shown in Figure (4.21c) and (4.21d) it is apparent that the FVM approaches the theoretical solution faster than the FEM as ϵ is reduced. The sensitivity of the solution accuracy due to this parameter for the FEM requires more investigation, particularly in the context of mesh refinement.

4.2.2 Dam-Break Flow over a Triangular Obstacle

The geometry for this test case has been previously shown in Figure (4.4). For the simulations, the uniform mesh spacing and time step are selected to be 0.1 and 0.004, respectively. Again, the FEM stabilization parameter δ_{s1} is utilized. As seen in Figures (4.22) and (4.23), comparable results and similar behavior between the FVM and FEM are observed. However, some notable differences are present. The water rise from the dam-break occurs sooner for the FEM on the frontal face of the triangular obstacle, as indicated in Figures (4.22b) and (4.22c). The behavior is reversed for the FVM at the apex of the triangular obstacle and downstream as shown in Figures (4.22d) and (4.22e), respectively.

Spatially, this behavior is readily seen in Figure (4.23) which displays the water height as a function of axial location for different time snapshots. Typically, numerical dissipation causes an inviscid solution to behave similar to one that has physical viscosity and, therefore, smear the discontinuity and cause it to appear upstream spatially or later temporally. From this observed behavior, the discrepancies between the computed results may be indicative of the FVM possessing more numerical dissipation than the FEM for this given discretization.

4.2.3 Parabolic Basin

In order to examine the performance of the new source-term balancing scheme introduced in the current FEM, the parabolic bowl case is considered and initialized with still water, i.e. $\zeta = 0$. Since the water is at rest, there is no motion in the bowl, and the water level should remain unchanged at each time step. Figure (4.24) indicates that the residual maintains machine zero as the equations are integrated in time and, therefore, the source-term balancing scheme does not disturb equilibrium. Note, this verification is necessary in order to ensure that the governing equations are satisfied both temporally and spatially for any implemented method.

The parabolic basis is again used for validation of the present FEM in accommodating moving wetting-drying interfaces with a non-flat bottom. The water surface is initialized with the exact solution given in equation (4.1), and a time step of $\Delta t = 0.001$ is utilized. In Figure (4.25), computed results are compared with both analytical and the current FVM solutions. Once again, comparable accuracy is observed between the two methodologies. Furthermore, regardless of numerical method used, based on the discretization utilized, error exists for wetting-drying problems due to the spurious water surface in partially-wet elements. Figures (4.25d) and (4.25f) illustrate this error where the bead of water intersects the parabolic bowl. In these figures, no discernable conclusions may be made concerning the superiority of one methodology over the other as the accuracy with the exact solution differs at the time snapshots. However, these errors are reduced as the mesh is refined in the vicinity of the interface.

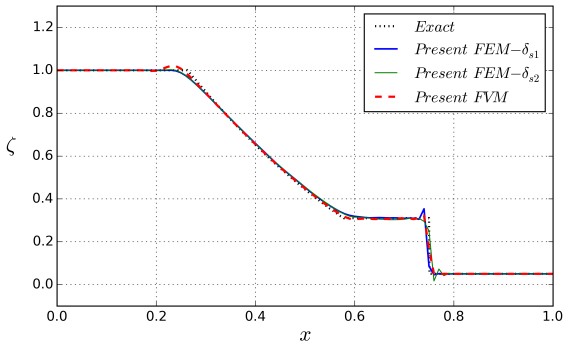

(a) Water Surface, Δs = 0.01

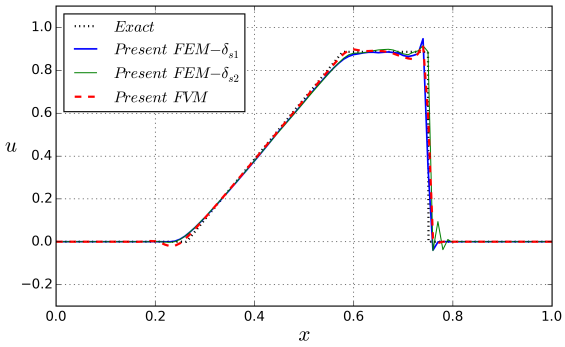

(b) Horizontal Velocity, Δs = 0.01

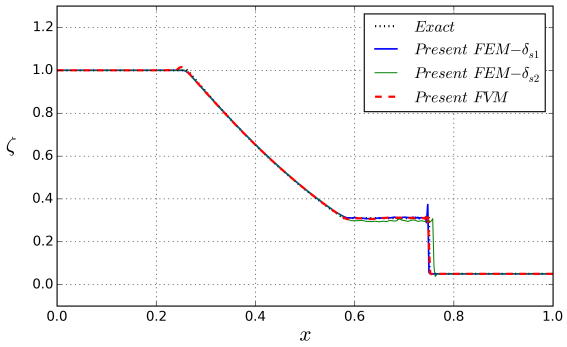

(c) Water Surface, Δs = 0.0025

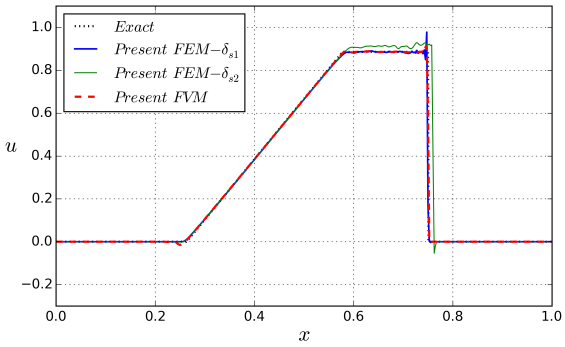

(d) Horizontal Velocity, Δs = 0.0025

Figure 4.20 The present FEM and FVM solutions for the wet-bed dam-break problem at t = 0.2366

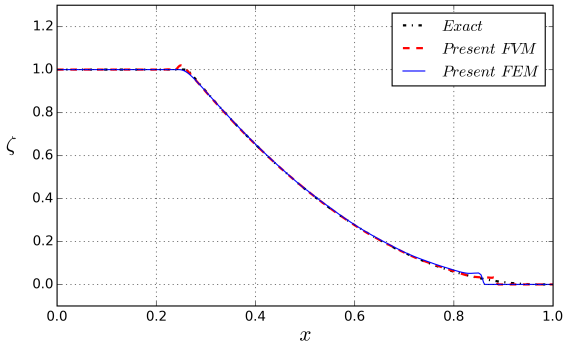

(a) Water Surface, $\epsilon = 10^{-3}$

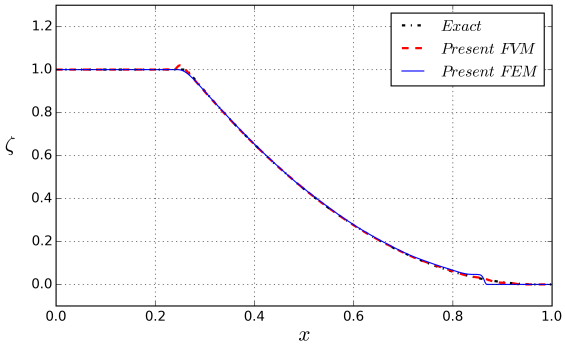

(b) Water Surface, $\epsilon = 10^{-5}$

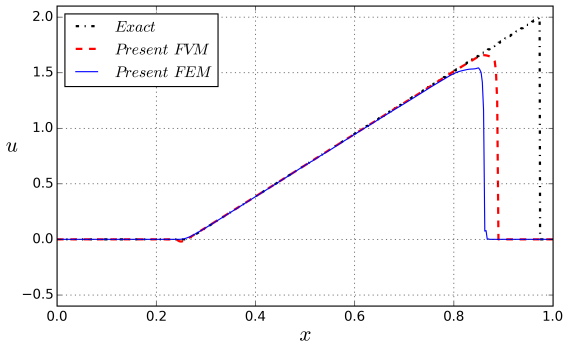

(c) Horizontal Velocity, $\epsilon = 10^{-3}$

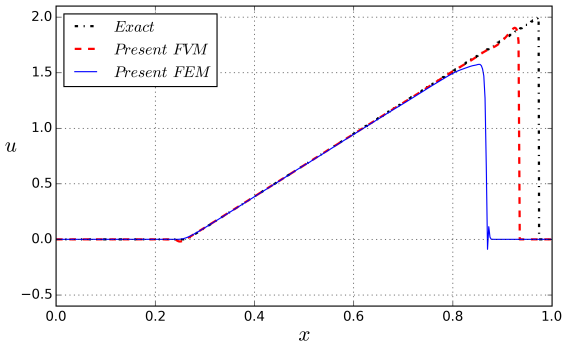

(d) Horizontal Velocity, $\epsilon = 10^{-5}$

Figure 4.21 The present FEM and FVM solutions for the dry-bed dam-break problem at t = 0.2366 ($\Delta s = 0.0025$)

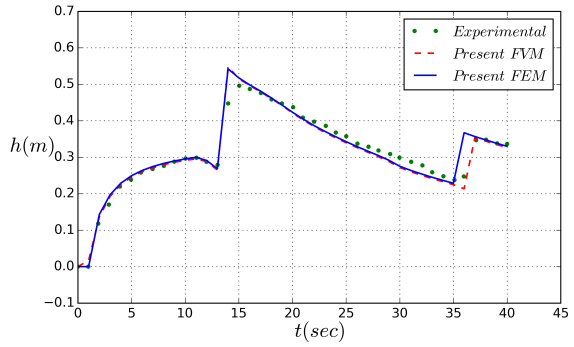

(a) G4

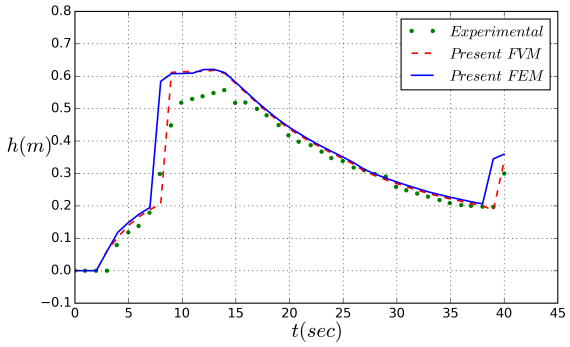

(b) G10

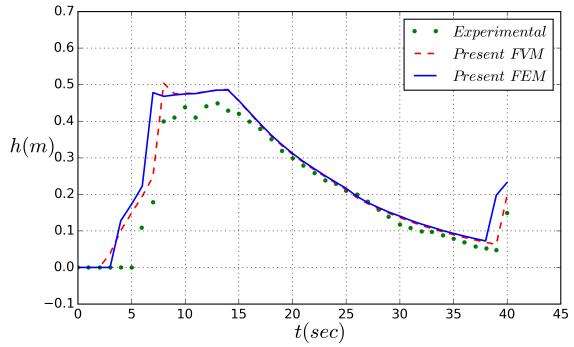

(c) G11

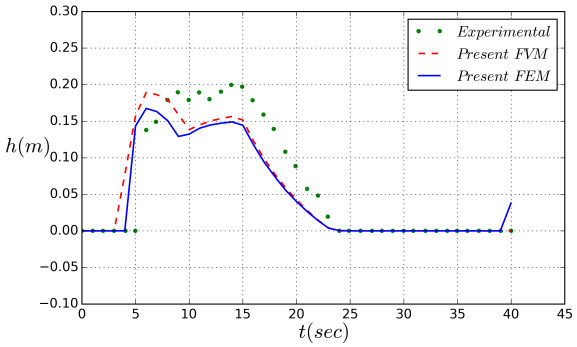

(d) G13

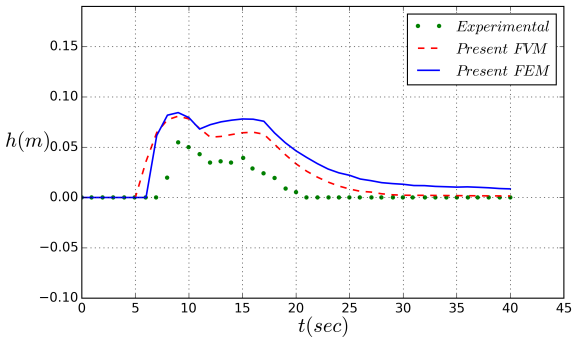

(e) G20

Figure 4.22 The present FEM and FVM solutions for the dam break flow over a triangular obstacle

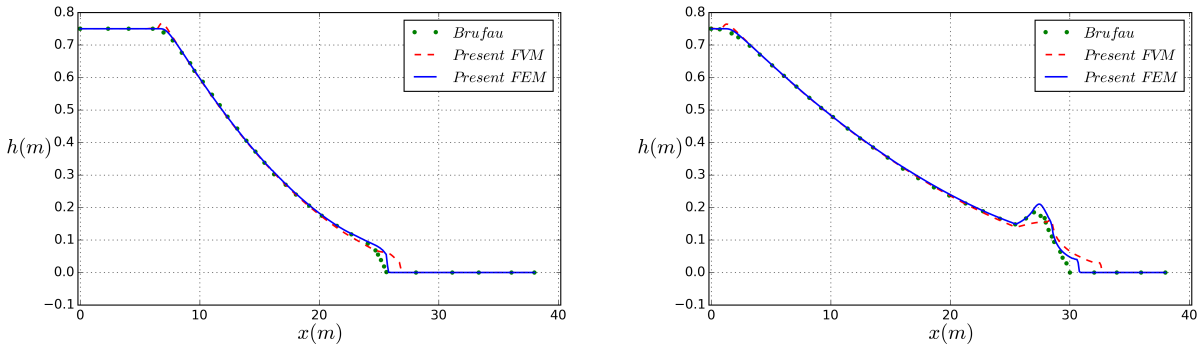

(a) t=3 sec

(b) t=5 sec

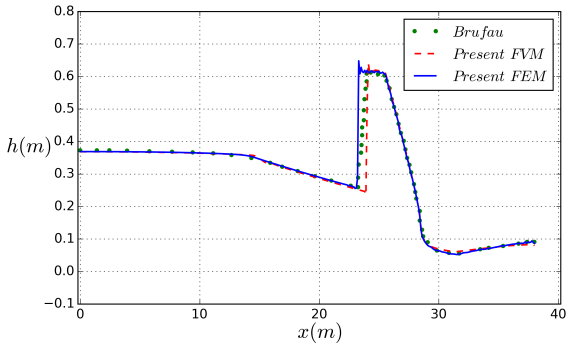

(c) t=10 sec

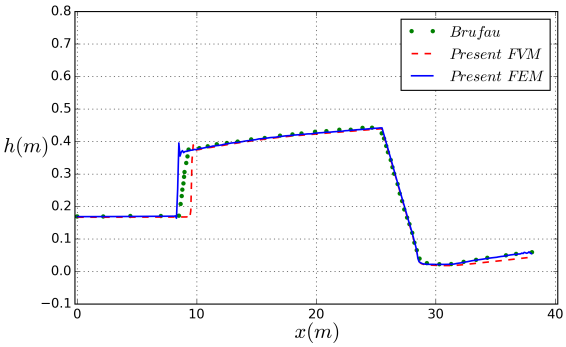

(d) t=20 sec

Figure 4.23 The present FEM and FVM solutions for the dam break flow over a triangular obstacle

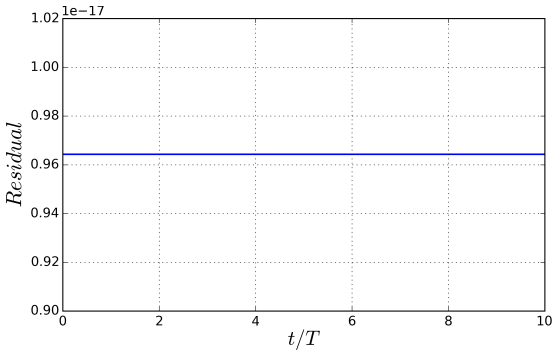

Figure 4.24 Residual for parabolic basin test case at rest

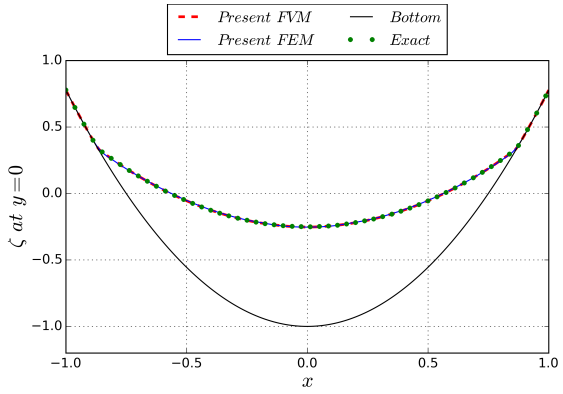

(a) t=4T/6

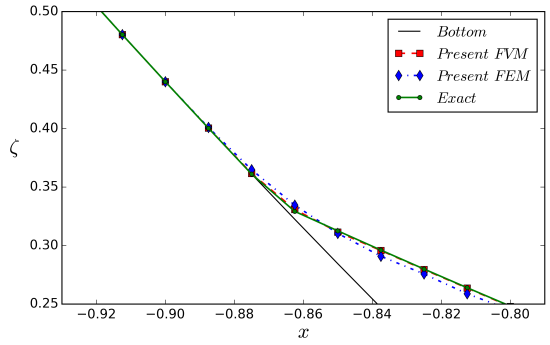

(b) details of solutions near the wet-dry interface in (a)

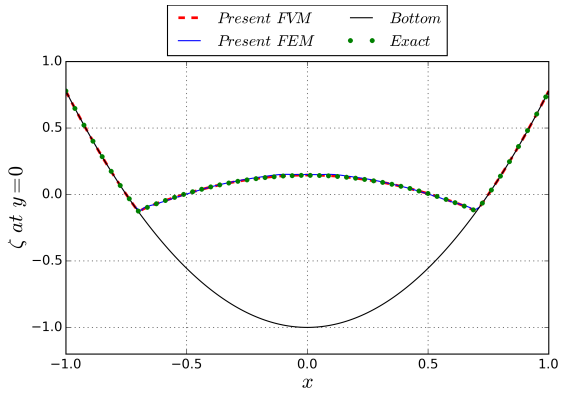

(c) t=5T/6

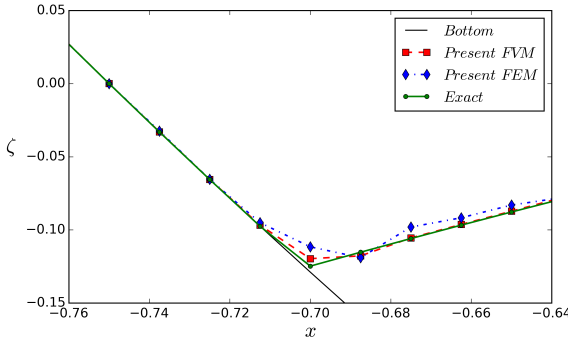

(d) details of solutions near the wet-dry interface in (c)

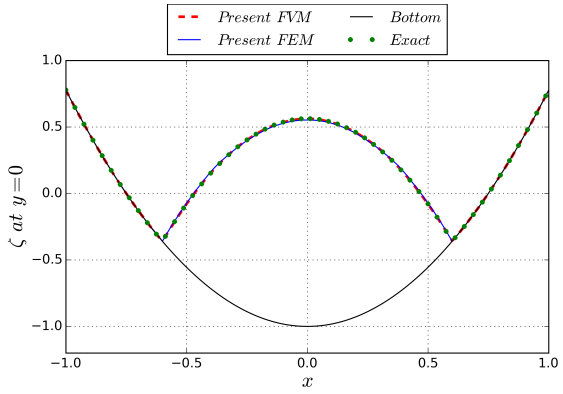

(e) t=T

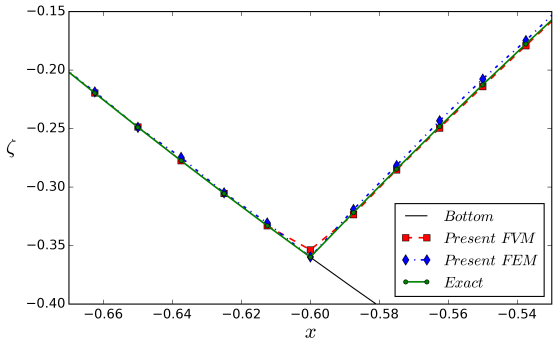

(f) details of solutions near the wet-dry interface in (e)

Figure 4.25 The present FEM and FVM solutions for the parabolic basin case ($\Delta s = 0.0125$)

4.2.4 Pollutant Advection

To examine the capability of the present FEM in simulating pollutant transport, the cavity test case introduced in Section 4.1.5 is repeated. The comparison of the two numerical methods with the exact solution is shown in Figure (4.27). Figures (4.27a) and (4.27b) illustrate the contaminant distribution at two time snapshots indicating qualitatively similar behavior. Furthermore, as seen in Figure (4.27c) both methods appear to have similar amounts of error. This is not the case as shown in Figure (4.27d) which is a near field view of the contaminant. To further examine the error in the presented methodologies, the total errors are computed based on the definition given in [66]. For pure advection, as described in [66], the total error may be defined as

$$E_{TOT} = \left[\sigma\left(q_E\right) - \sigma\left(q_N\right)\right]^2 + \left(\bar{q_E} - \bar{q_N}\right)^2 + 2\left(1-\rho\right)\sigma\left(q_E\right)\sigma\left(q_N\right) \tag{4.8}$$

where q_E and q_N are the exact and numerical solutions respectively, σ is the variance, and ρ is the correlation coefficient between q_E and q_N. If the exact and numerical solutions are perfectly correlated then $\rho = 1$, and the only error in the simulation is due to dissipation. Thus, the dissipation error may be defined as

$$E_{DISS} = \left[\sigma\left(q_E\right) - \sigma\left(q_N\right)\right]^2 + \left(\bar{q_E} - \bar{q_N}\right)^2 \tag{4.9}$$

Furthermore, a dispersion error is introduced for $\rho \neq 1$ and therefore may be defined by

$$E_{DISP} = 2\left(1-\rho\right)\sigma\left(q_E\right)\sigma\left(q_N\right) \tag{4.10}$$

Using these definitions, Table (4.3) quantitatively indicates that the FEM possesses significantly less dissipation errors, as well as smaller dispersion errors than the FVM for the given discretization.

Table 4.3 Dissipation and Dispersion errors for the pollutant advection case

Numerical Method	ρ	*Dissipation Error*	*Dispersion Error*	*Total Error*
FVM	0.995	8.075e-05	3.119e-02	3.127e-02
FEM	0.997	4.441e-09	1.765e-02	1.765e-02

4.2.5 Isolated Building Benchmark

The benchmark problem from [67] is considered to again validate the current FV and FE methodologies with experimental data. In this problem, a dam-break flow with a building downstream of the dam is simulated. As shown in Figure (4.26), the problem domain consists of a reservoir and a channel with a gate between them located at $x = 0$, and a single building downstream of the gate. The wall boundary condition is imposed for all boundaries except the outflow boundary. A water depth of $0.4\,m$ in the upstream reservoir and a thin layer of $0.01\,m$ in the downstream channel are implemented as the initial condition at $t = 0$. The Manning coefficient is $n = 0.01\,s.m^{-1/3}$ and the parameter used to avoid singularities in dry regions is $\epsilon = 0.001$. The water level is recorded at each time step in several gauges located as seen in Figure (4.26). Table (4.4) gives the exact location of each gauge.

This test case was also simulated by six different institutions and their results are compared to the experimental data in [67]. The experiments were carried out in the laboratory of the Civil and Environmental Engineering Department of the Université Catholique de Louvain (UCL) in Belgium. The experimental results are obtained within the first 30 seconds after the dam breaks

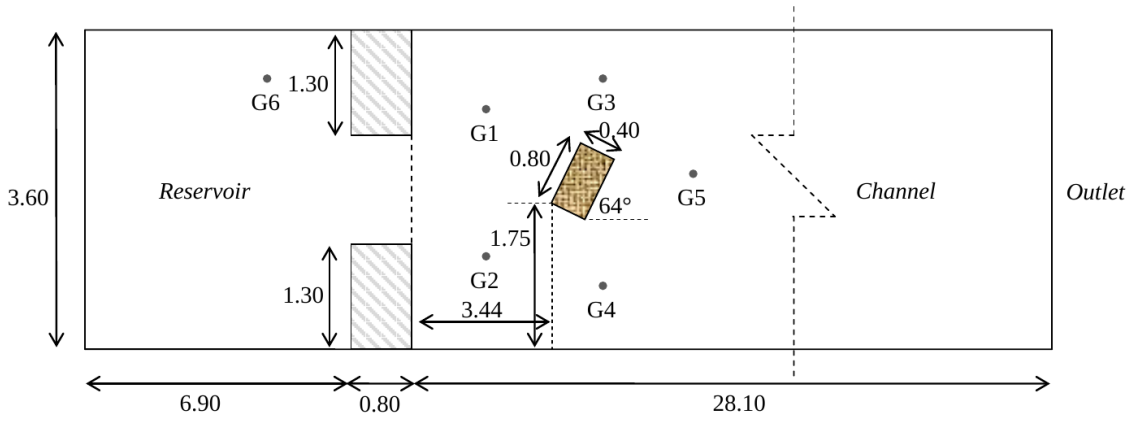

(a) Plan view

(b) Cross section

Figure 4.26 The problem geometry for the isolated building test case

and hence the numerical results are also computed within the same time interval. The time step used in the current simulation is $\Delta t = 0.01$. To validate the numerical results of the present work, the water-level history at each gauge is compared to the experimental results.Additionally, results from other simulation codes, as presented in [67], are also shown for comparative purposes.

The water height as a function of time at gauge 6 is shown in Figure (4.28). This gauge is placed upstream of the dam in order to monitor the water level drop within the reservoir. As seen in Figure (4.28a), both of the current solution methodologies match the experimental data very well. Furthermore, similar agreement is also observed from the simulation techniques found in [67] and

Table 4.4 Gauge locations for the isolated building case

Gauge number	$x(m)$	$y(m)$
G1	2.65	1.15
G2	2.65	-0.60
G3	4.00	1.15
G4	4.00	-0.80
G5	5.20	0.30
G6	-1.87	1.10

given in Figure (4.28b). Note, in this and similar figures, the gauge locations are indicated in an insert for reference.

For gauge 1, as shown in Figure (4.29), the water height is affected by waves reflecting from the upper wall as well as the oblique face of the building. This can be observed in the experimental data by the arrival of the water from the reservoir at approximately 1 sec, instantaneously raising the water level to approximately 0.06 m, immediately followed by a reflection from the upper surface doubling the height. Subsequently, the influence of the building can be observed by the irregular water surface for the remainder of the simulation. Discrepancies between the two solution methodologies and the experimental data are apparent in Figure (4.29a), and may indicate that greater mesh refinement and a much smaller time step could be required to resolve this interaction. However, as seen in Figure (4.29b), other simulation software incurred similar discrepancies for this gauge location. Overall, the current FVM and FEM schemes appear comparable in accuracy to those in [67].

For gauge 2 shown in Figure (4.30), which is directly below gauge 1, the experimental data again indicates the arrival of the water from the reservoir at approximately 1 sec. However, this gauge location illustrates the effect of the building in producing a hydraulic jump. The FVM predicts this hydraulic jump at a much later time than the FEM, which may indicate that the FVM

possesses more dissipation and dispersion errors for the given discretization. Comparing Figure (4.30a) using the current methodologies, and Figure (4.30b) with the other simulation software, many of those schemes only predict the initial water rise and are not capable of resolving the hydraulic jump.

Depicted in Figure (4.31) are the simulated results for gauge 3. This gauge location is between the upper wall and an oblique building face. The building face is directed away from the gauge. As such, Figure (4.31b) illustrates the reflections of the waves off of these surfaces of the integrated time. However, the water level rise from the initial wave from reservoir is more uniform in nature. This behavior is similarly predicted by all the software presented in [67].

Similar to gauge 1, Figure (4.32) for gauge 4 demonstrations the arrival of the initial water from the reservoir followed by the interaction of the waves emanating from the building wall. The current methodologies do not adequately capture this interaction from the initial reflection from the building as seen in Figure (4.32a). This may indicate that greater mesh resolution is required in this region. In Figure (4.32b) only one code appears to predict this reflection reasonably well, however, the water height and subsequent interaction is vastly under predicted.

Finally, the computed results at gauge 5 are presented in Figure (4.33). This gauge is located directly downstream of the building and is greatly affected by the wake. As seen in Figure (4.33a), the FEM appears to predict the water heights more accurately than the FVM in this region. Furthermore, Figure (4.33b) indicates that most of the software used in [67] do not capture the water height fluctuations that are dominant in the wake. This again may be observed in Figure (4.34) which presents the experimental and computed velocities at gauge 5. The current FVM in

Figure (4.34a), and those presented from the other software in Figure (4.34b), illustrates under prediction of the water velocity and with very little variation over the integration time.

As a qualitative illustration of the complex wave pattern resulting from the dam-break flow impacting a downstream building, the computed water depth contours are shown in Figure (4.35) at several time snapshots. As is apparent in Figure (4.35a) at 1 sec, the water from the reservoir has reached gauges 1 and 2. Figure (4.35b) illustrates the wave pattern shortly after the isolated building is impacted and the reflection from the upper wall has occurred. In this figure, the separate waves can be clearly seen. At a time of 10 seconds, presented in Figure (4.35c), the large wave, described as a hydraulic jump in the discussion of Figure (4.30), is observed approaching gauge 2. Finally, in Figure (4.35d), the reservoir is at half the initial water height and the flow is seen to be interacting with the wall and building geometry.

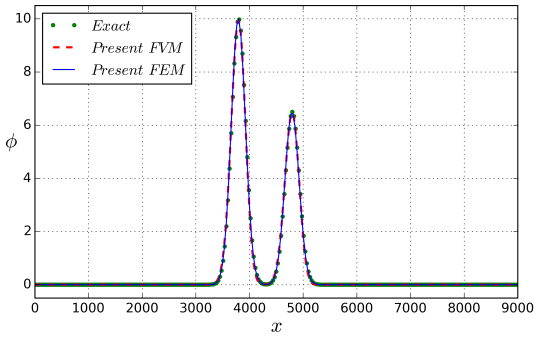

(a) Contaminant distribution at t = 4800 sec

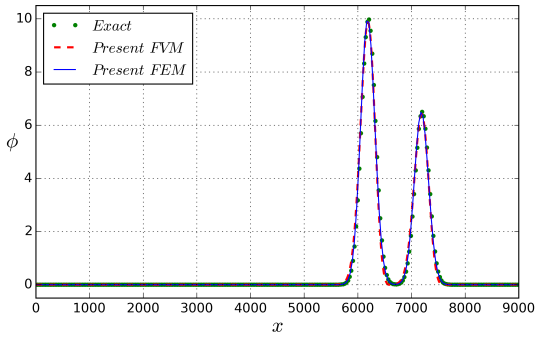

(b) Contaminant distribution at t = 9600 sec

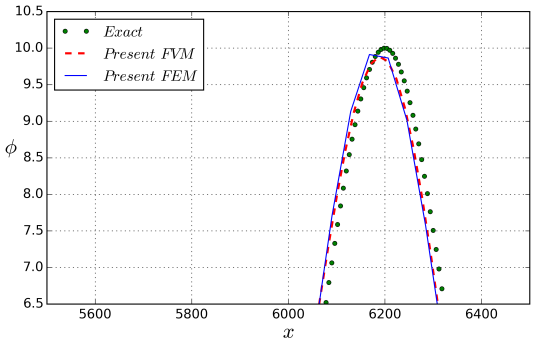

(c) Details of solutions at t = 9600 sec

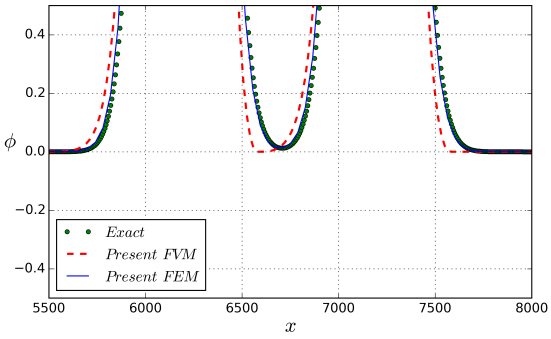

(d) Details of solutions at t = 9600 sec

Figure 4.27 The present FEM and FVM solutions for the contaminant transport case

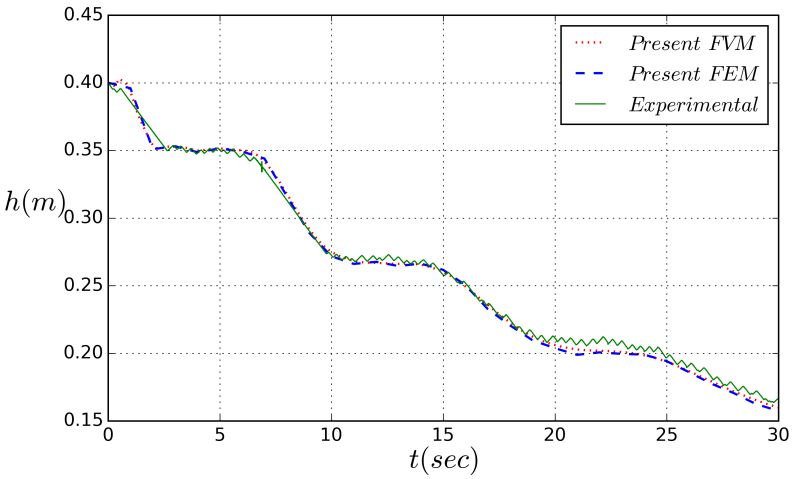

(a) G6 - present work

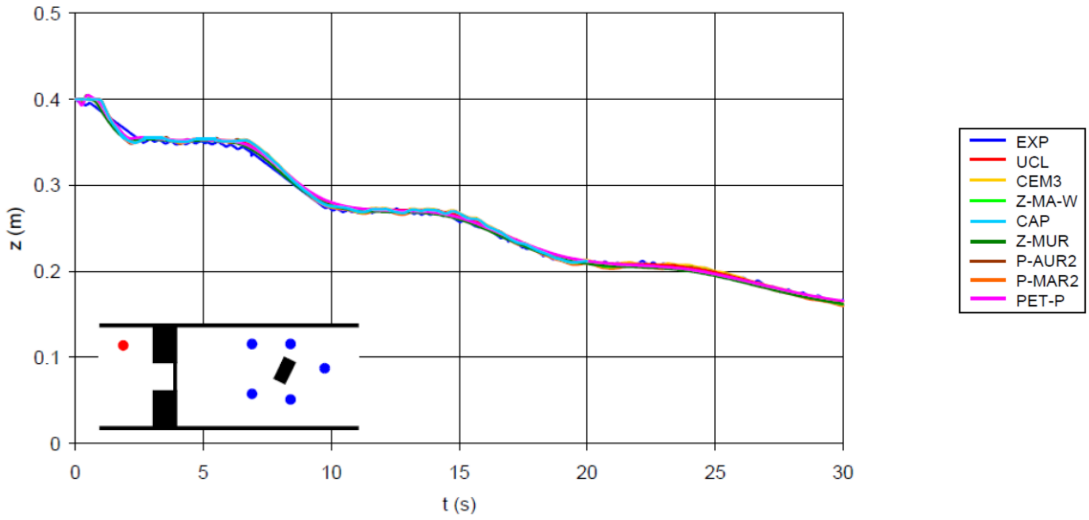

(b) G6 - other works

Figure 4.28 The experimental and numerical water depth at G6

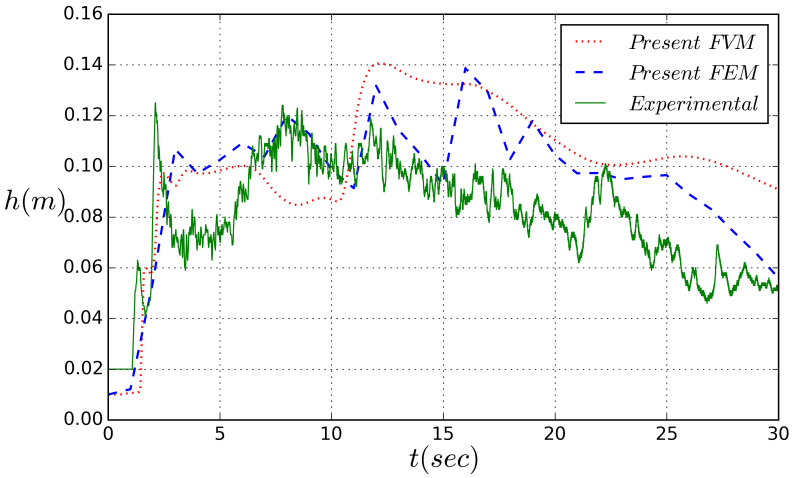

(a) G1 - present work

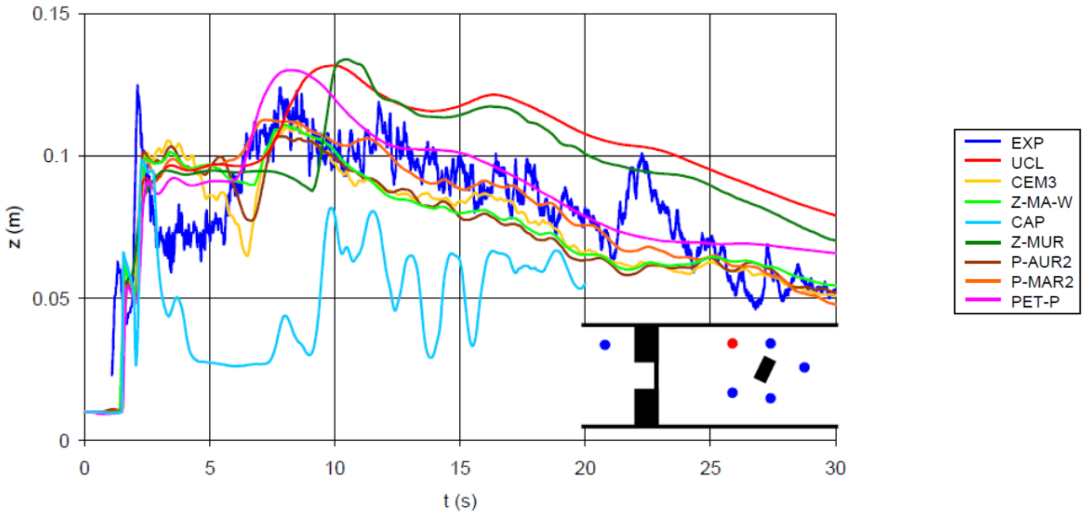

(b) G1 - other works

Figure 4.29 The experimental and numerical water depth at G1

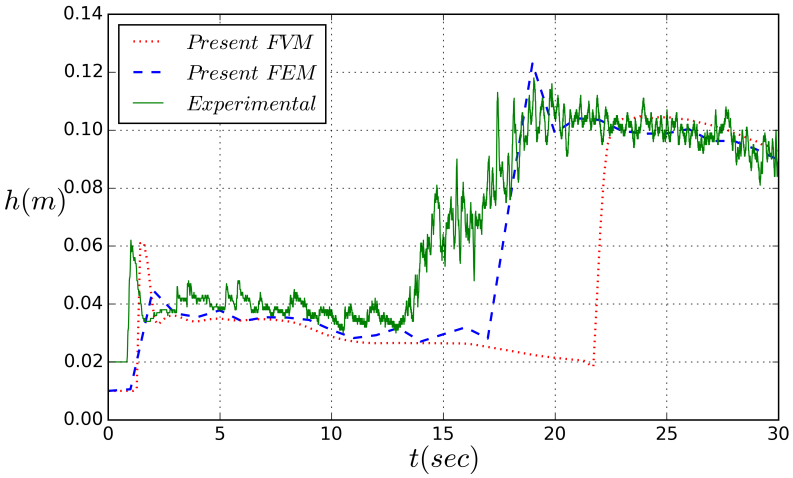

(a) G2 - present work

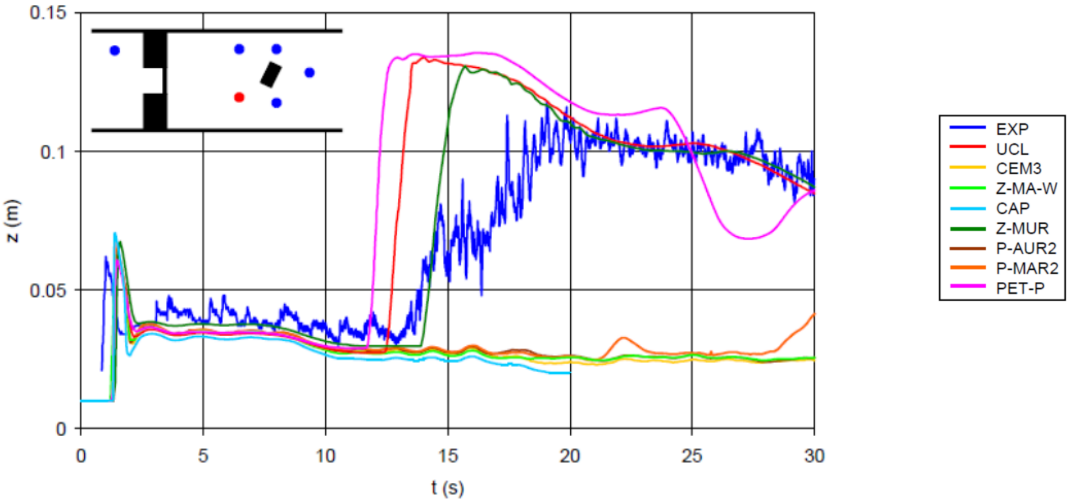

(b) G2 - other works

Figure 4.30 The experimental and numerical water depth at G2

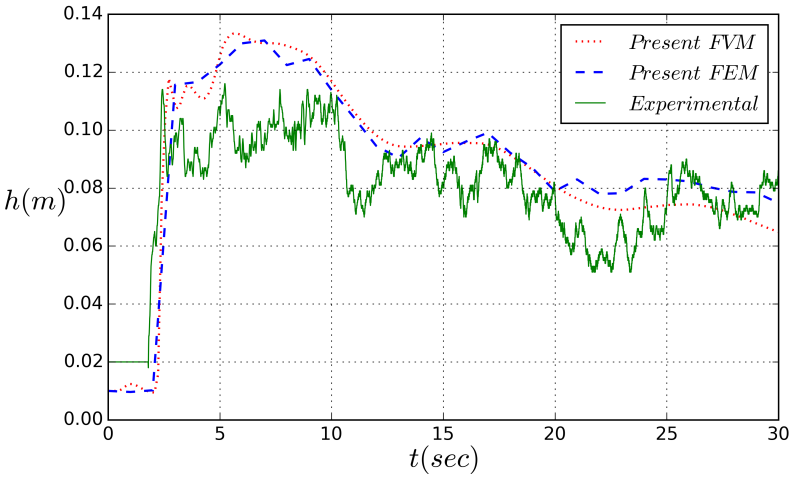

(a) G3 - present work

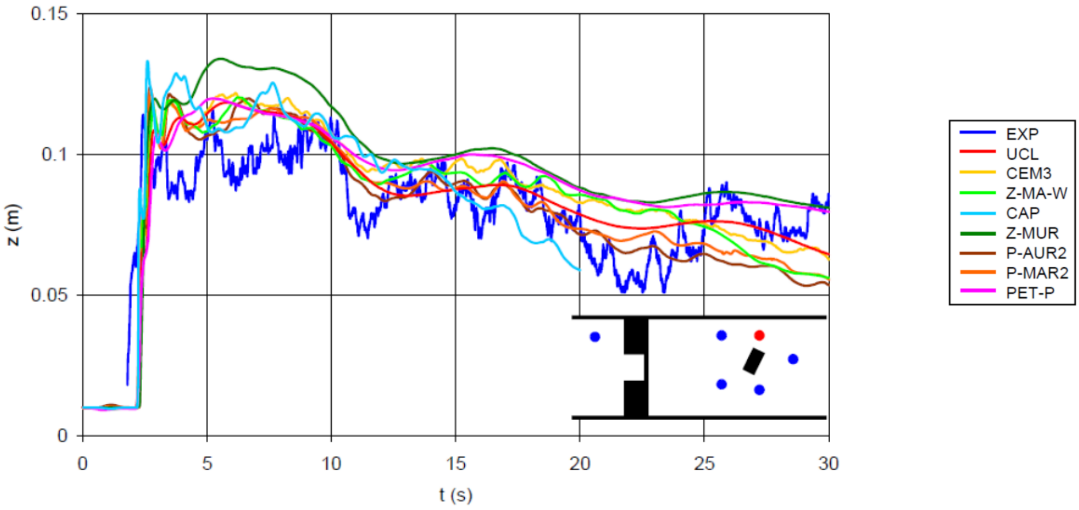

(b) G3 - other works

Figure 4.31 The experimental and numerical water depth at G3

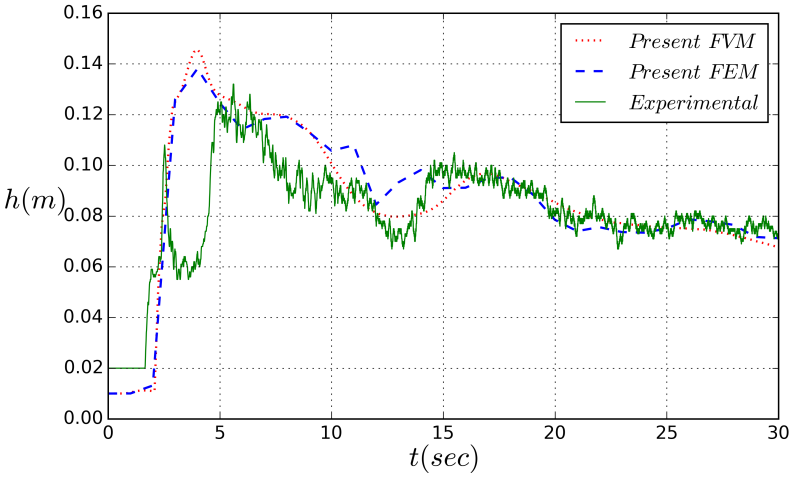

(a) G4 - present work

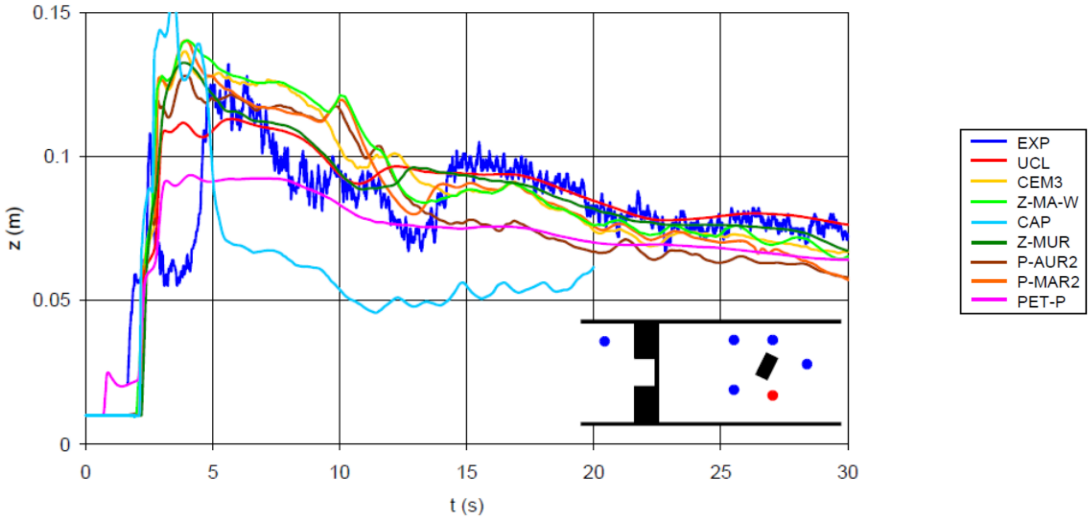

(b) G4 - other works

Figure 4.32 The experimental and numerical water depth at G4

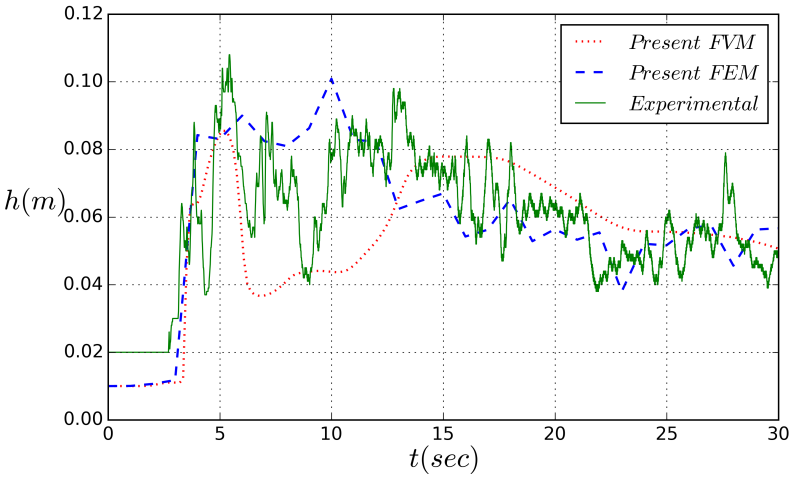

(a) G5 - present work

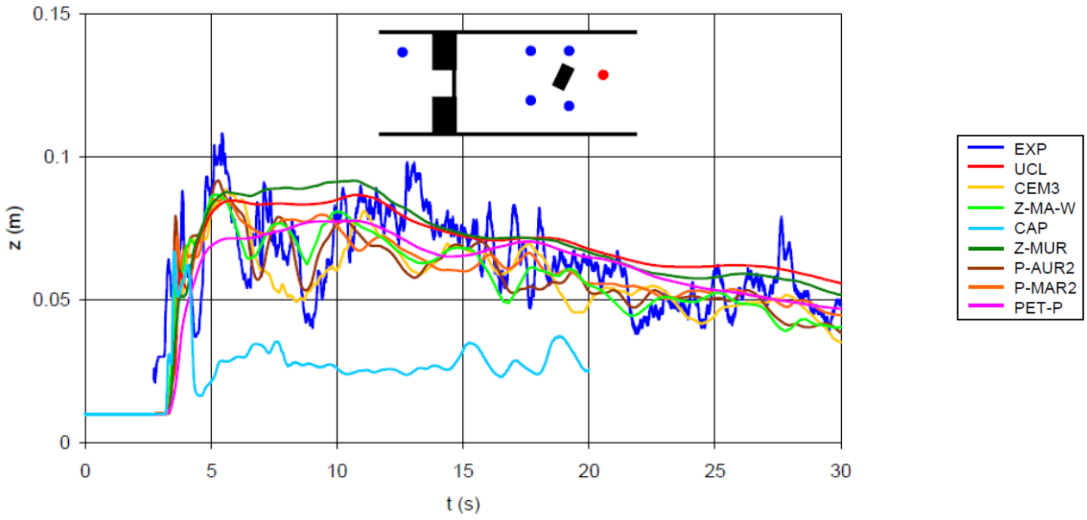

(b) G5 - other works

Figure 4.33 The experimental and numerical water depth at G5

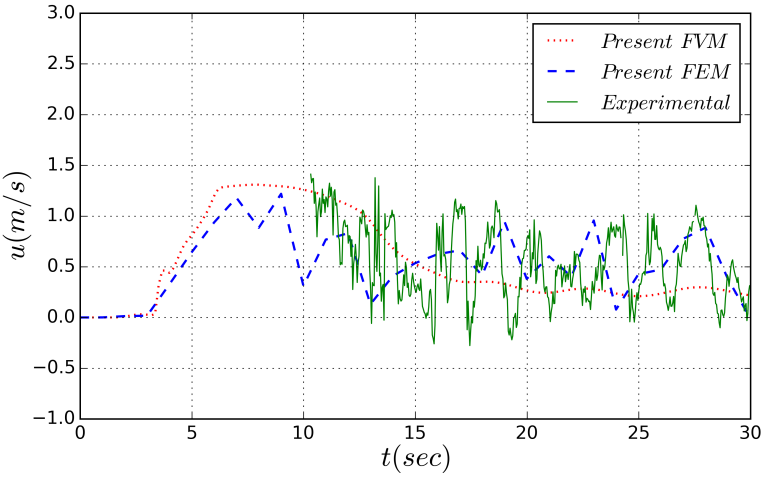

(a) G5 - present work

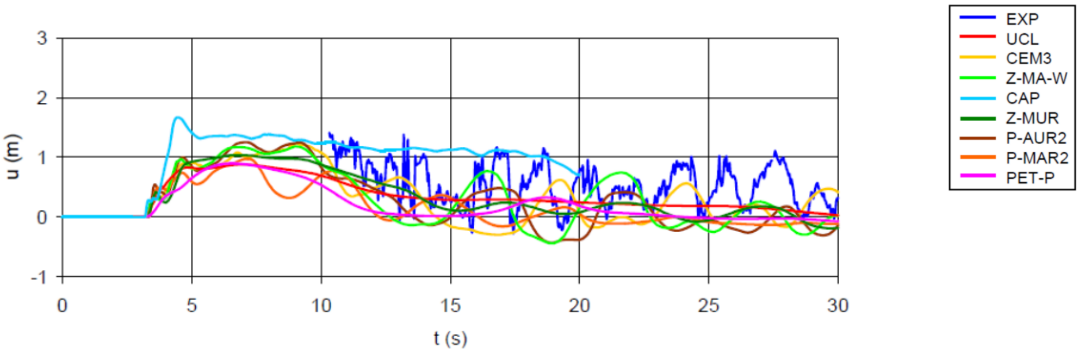

(b) G5 - other works

Figure 4.34 The experimental and numerical velocity at G5

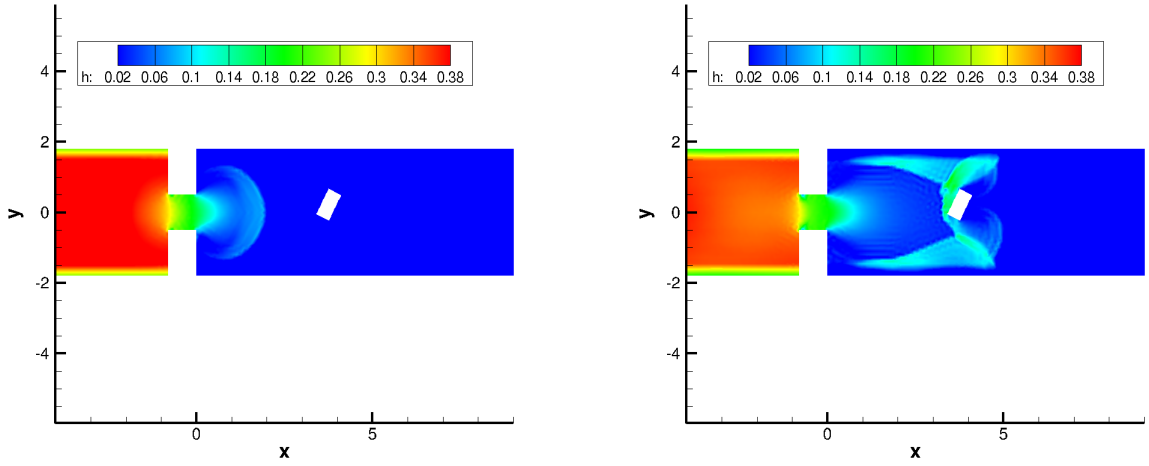

(a) t=1 sec

(b) t=3 sec

(c) t=10 sec

(d) t=20 sec

Figure 4.35 The computed water depth contours near the building

CHAPTER 5

CONCLUSIONS

A primitive-variable Riemann solver and a semi-discrete SUPG method were developed and validated for the fully-coupled shallow water and contaminant transport equations. The primitive-variable model is an extension of the finite volume approach proposed in [8] and in particular focuses on ability to simulate contaminant transport. In the finite element framework, a new source-term balancing scheme is introduced to accommodate arbitrary bed topography and wetting-drying fronts. Utilizing various test problems with flat and non-flat beds, dry regions, and still-water surface it was demonstrated that the developed numerical schemes accurately simulate flow properties as well as pollutant advection and diffusion. Additionally, the finite volume model was used for the pollutant transport following a flood, and indicated that the algorithm is stable and robust in simulating the flow dynamics and contaminant transport in real-world cases.

The present numerical schemes are implemented on fixed computational meshes. Hence, simulating wetting-drying interfaces in a FEM context leads to the existence of partially-wet elements which are sources of numerical errors. In the present work, this type of error is eliminated for still-water problems and may be reduced for moving boundary problems by using mesh refinement. Since a node-centered paradigm is applied in the present FVM, partially-wet elements do not present numerical difficulties.

CHAPTER 6

FUTURE WORK

The current work presents the development and validation of two numerical methodologies to predict the flow and pollutant transport using the fully-coupled shallow water and contaminant transport equations. To continue this research, a more detailed analysis of the error sources is needed in order to investigate their impact on solution accuracy. To improve solution accuracy, the current FEM is readily extendable to higher orders of spatial accuracy. The path forward for higher order spatial accuracy is not feasible with the FVM. Furthermore, adaptive mesh refinement (h-, p-, and hp-adaptation) techniques should be explored within the FEM context. Additionally, higher-order temporally accurate schemes should be investigated. From the results presented for the isolated building case in Section 4.2.5, the water heights and velocities exhibited high frequency variations both spatially and temporally. Solution accuracy may be greatly increase by investigating higher-order methods as a result. The focus of the current research was the development and validation of both FVM and FEM methodologies for this particular flow regime. However, the computational efficiency, particularly for the current FEM, should be considered and improved. Although outside the focus of the current research, the embarrassingly parallel nature of the finite element solution methodology could be exploited for significant simulation time reductions.

REFERENCES

[1] García-Navarro, P., Playán, E., and Zapata, N., "Solute transport modelling in overland flow applied to fertigation," *Journal of Irrigation and Drainage Engineering*, Vol. 126, No. 1, 2000, pp. 33–40.

[2] Wu, W., Vieira, D. A., and Wang, S. S., "One-dimensional numerical model for nonuniform sediment transport under unsteady flows in channel networks," *Journal of Hydraulic Engineering*, Vol. 130, No. 9, 2004, pp. 914–923.

[3] Li, S. and Duffy, C. J., "Fully-coupled modeling of shallow water flow and pollutant transport on unstructured grids," *Procedia Environmental Sciences*, Vol. 13, 2012, pp. 2098–2121.

[4] Bermudez, A. and Vázquez-Cendón, M., "Upwind methods for hyperbolic conservation laws with source terms," *Computers and Fluids*, Vol. 23, No. 8, 1994, pp. 1049–1071.

[5] Medeiros, S. and Hagen, S., "Review of wetting and drying algorithms for numerical tidal flow models," *International Journal for Numerical Methods in Fluids*, Vol. 71, 2013, pp. 473–487.

[6] Rogers, B., Fujihara, M., and Borthwick, A., "Adaptive Q-tree Godunov-type scheme for shallow water equations," *International Journal for Numerical Methods in Fluids*, Vol. 35, 2001, pp. 247–280.

[7] Rogers, B., Borthwick, A., and Taylor, P., "Mathematical balancing of flux gradient and source terms prior to using Roe's approximate Riemann solver," *Journal of Computational Physics*, Vol. 192, 2003, pp. 422–451.

[8] Sivakumar, P., Hyams, D. G., Taylor, L. K., and Briley, W. R., "A primitive-variable Riemann method for solution of the shallow water equations with wetting and drying," *Journal of Computational Physics*, Vol. 228, No. 19, 2009, pp. 7452–7472.

[9] Weiyan, T., *Shallow Water Hydrodynamics: Mathematical Theory and Numerical Solution for a Two-dimensional System of Shallow Water Equations*, Elsevier Science Publishing Company, New York, 1992.

[10] Loukili, Y. and Soulaimani, A., "Numerical tracking of shallow water waves by the unstructured finite volume WAF approximation," *International Journal for Computational Methods in Engineering Science and Mechanics*, Vol. 8, No. 2, 2007, pp. 75–88.

[11] Toro, E. F., *Shock Capturing Methods for Free-Surface Shallow Flows*, John Wiley and Sons, Ltd.,New York, 2001.

[12] Liang, Q. and Borthwick, A., "Adaptive quadtree simulation of shallow flows with wet-dry fronts over complex topography," *Computers and Fluids*, Vol. 38, 2009, pp. 221–234.

[13] Liang, Q. and Marche, F., "Numerical resolution of well-balanced shallow water equations with complex source terms," *Advances in Water Resources*, Vol. 32, 2009, pp. 873–884.

[14] Hou, J., Simons, F., Mahgoub, M., and Hinkelmann, R., "A robust well-balanced model on unstructured grids for shallow water flows with wetting and drying over complex topography," *Computer Methods in Applied Mathematics and Engineering*, Vol. 257, 2013, pp. 126–149.

[15] Hou, J., Liang, Q., Simons, F., and Hinkelmann, R., "A 2D well-balanced shallow flow model for unstructured grids with novel slope source term treatment," *Advances in Water Resources*, Vol. 52, 2013, pp. 107–131.

[16] Horváth, Z., Waser, J., Perdigão, R., Konev, A., and Blöschl, G., "A two-dimensional numerical scheme of dry/wet fronts for theSaint-Venant system of shallow water equations," *International Journal for Numerical Methods in Fluid*, Vol. 77, 2015, pp. 159–182.

[17] Guan, M., Wright, N., and P.A.Sleigh, "A robust 2D shallow water model for solving flow over complextopography using homogenous flux method," *International Journal for Numerical Methods in Fluid*, Vol. 73, 2013, pp. 225–249.

[18] Duran, A., "A robust and well-balanced scheme for the 2D Saint-Venant system on unstructured meshes with friction source term," *International Journal for Numerical Methods in Fluids*, Vol. 78, 2015, pp. 89–121.

[19] Bradford, S. and Sanders, B., "Finite-volume model for shallow-water flooding of arbitrary topography," *Journal of Hydraulic Engineering*, Vol. 128, 2002, pp. 289–298.

[20] Murillo, J., Burguete, J., Brufau, P., and García-Navarro, P., "Coupling between shallow water and solute flow equations: analysis and management of source terms in 2D," *International Journal for Numerical Methods in Fluids*, Vol. 49, No. 3, 2005, pp. 267–299.

[21] Murillo, J., García-Navarro, P., Burguete, J., and Brufau, P., "A conservative 2D model of inundation flow with solute transport over dry bed," *International Journal for Numerical Methods in Fluids*, Vol. 52, 2006, pp. 1059–1092.

[22] Murillo, J., García-Navarro, P., and Burguete, J., "Analysis of a second-order upwind method for the simulationof solute transport in 2D shallow water flow," *International Journal for Numerical Methods in Fluids*, Vol. 56, 2008, pp. 661–686.

[23] Begnudelli, L. and Sanders, B. F., "Unstructured grid finite-volume algorithm for shallow-water flow and scalar transport with wetting and drying," *Journal of Hydraulic Engineering*, Vol. 132, No. 4, 2006, pp. 371–384.

[24] Benkhaldoun, F., Elmahi, I., and Seaid, M., "Well-balanced finite volume schemes for pollutant transport on unstructured meshes," *Journal of Computational Physics*, Vol. 226, No. 1, 2007, pp. 180–203.

[25] Cea, L. and Vázquez-Cendón, M., "Unstructured finite volume discretisation of bed friction and convective flux in solute transport models linked to the shallow water equations," *Journal of Computational Physics*, Vol. 231, 2012, pp. 3317–3339.

[26] Bunya, S., Kubatko, E., Westerink, J., and Dawson, C., "A wetting and drying treatment for the Runge-Kutta discontinuous Galerkin solution to the shallow water equations," *Computer Methods in Applied Mechanics and Engineering*, Vol. 198, 2009, pp. 1548–1562.

[27] Takase, S., Kashiyama, K., Tanaka, S., and Tezduyar, T., "Space-time SUPG formulation of the shallow-water equations," *International Journal for Numerical Methods in Fluids*, Vol. 64, 2010, pp. 1379–1394.

[28] Takase, S., Kashiyama, K., Tanaka, S., and Tezduyar, T., "Space-time SUPG finite element computation of shallow-water flows with moving shorelines," *Computational Mechanics*, Vol. 48, 2011, pp. 293–306.

[29] Zhao, L., Guo, B., Li, T., Avital, E., and Williams, J., "A well-balanced explicit/semi-implicit finite element scheme for shallow water equations in drying-wetting areas," *International Journal for Numerical Methods in Fluids*, Vol. 75, 2014, pp. 815–834.

[30] Porta, G., Perotto, S., and Ballio, F., "A space-time adaptation scheme for unsteady shallow water problems," *Mathematics and Computers in Simulation*, Vol. 82, 2012, pp. 2929–2950.

[31] Heniche, M., Secretan, Y., Boudreau, P., and Leclerc, M., "A two-dimensional finite element drying-wetting shallow water model for rivers and estuaries," *Advances in Water Resources*, Vol. 23, 2000, pp. 359–372.

[32] Lai, W. and Khan, A., "A discontinuous Galerkin method for two-dimensional shallow water flows," *International Journal for Numerical Methods in Fluids*, Vol. 70, 2012, pp. 939–960.

[33] Xing, Y. and Zhang, X., "Positivity-preserving well-balanced discontinuous Galerkin methods for the shallow water equations on unstructured triangular meshes," *Journal of Scientific Computing*, Vol. 57, 2013, pp. 19–41.

[34] Aizinger, V. and Dawson, C., "A discontinuous Galerkin method for two-dimensional flow and transport in shallow water," *Advances in Water Resources*, Vol. 25, 2002, pp. 67–84.

[35] Ortiz, P., "Shallow water flows over flooding areas by a flux-corrected finite element method," *Journal of Hydraulic Research*, Vol. 52, 2014, pp. 241–252.

[36] Remacle, J., Frazao, S., Li, X., and Shephard, M., "An adaptive discretization of shallow-water equations based on discontinuous Galerkin methods," *International Journal for Numerical Methods in Fluids*, Vol. 52, 2006, pp. 903–923.

[37] Hauke, G., "A symmetric formulation for computing transient shallow water flows," *Computer Methods in Applied Mechanics and Engineering*, Vol. 163, 1998, pp. 111–122.

[38] Brooks, A. and Hughes, T., "Streamline upwind/petrov-galerkin formulations for convection dominated flows with particular emphasis on the incompressible navier-stokes equations," *Computer Methods in Applied Mechanics and Engineering*, Vol. 32, 1982, pp. 199–259.

[39] Tezduyar, T. and Hughes, T., "Development of time-accurate finite element techniques for first-order hyperbolic systems with particular emphasis on the compressible Euler equations," Tech. rep., NASA-CR-204772, 1982.

[40] Hughes, T. and Tezduyar, T., "Finite element methods for first-order hyperbolic systems with particular emphasis on the compressible Euler equations," *Computer Methods in Applied Mechanics and Engineering*, Vol. 45, 1984, pp. 217–284.

[41] Tezduyar, T. and Hughes, T., "Finite element formulations for convection dominated flows with particular emphasis on the compressible Euler equations," *AIAA 83-0125*, 1983.

[42] Hughes, T. and Mallet, M., "A new finite element formulation for computational fluid dynamics: IV. A discontinuity-capturing operator for multidimentional advective-diffusive systems," *Computer Methods in Applied Mechanics and Engineering*, Vol. 58, 1986, pp. 329–336.

[43] Bova, S. and Carey, G., "A symmetric formulation and SUPG scheme for the shallow-water equations," *Advances in Water Resources*, Vol. 19, 1996, pp. 123–131.

[44] Hughes, T. and Mallet, M., "A new finite element formulation for computational fluid dynamics: III. The generalized streamline operator for multidimensional advective-diffusive systems," *Computer Methods in Applied Mechanics and Engineering*, Vol. 58, 1986, pp. 305–328.

[45] Tezduyar, T., *Encyclopedia of Computational Mechanics*, Vol. 3, John Wiley & Sons, Ltd, 2004.

[46] Tezduyar, T., "Finite elements in fluids: stabilized formulations and moving boundaries and interfaces," *Computers and Fluids*, Vol. 36, 2007, pp. 191–206.

[47] Tezduyar, T. and Senga, M., "Stabilization and shock-capturing parameters in SUPG formulation of compressible flows," *Computer Methods in Applied Mechanics and Engineering*, Vol. 195, 2006, pp. 1621–1632.

[48] Bates, P. and Horritt, M., *Computational Fluid Dynamics: Applications in Environmental Hydraulics*, John Wiley & Sons, Ltd, 2005.

[49] Bates, P. and Hervouet, J., "A new method for moving-boundary hydrodynamic problems in shallow water," *Mathematical, Physical and Engineering Sciences*, Vol. 455, 1999, pp. 3107–3128.

[50] Caleffi, V. and Valiani, A., "A 2D local discontinuous Galerkin method for contaminant transport in channel bends," *Computers and Fluids*, Vol. 88, 2013, pp. 629–642.

[51] Hyams, D. G., *An investigation of parallel implicit solution algorithms for incompressible flows on unstructured topologies*, Ph.D. Thesis Mississippi State University, 2000.

[52] Anderson, W. K. and Bonhaus, D. L., "An implicit upwind algorithm for computing turbulent flows on unstructured grids," *Computers and Fluids*, Vol. 23, No. 1, 1994, pp. 1–21.

[53] Swafford, T. W., *Notes for Computational Fluid Dynamics*, SimCenter National Center for Computational Engineering, 2011.

[54] Whitfield, D. and L.K.Taylor, "Discretized Newton-relaxation solution of high resolution flux-difference split schemes," *AIAA Paper 91-1539*, 1991.

[55] Taylor, L. and Whitfield, D., "Unsteady three-dimensional incompressible Euler and Navier-Stokes solver for stationary and dynamic grids," *AIAA Paper 91-1650*, 1991.

[56] Squire, W. and Trapp, G., "Using complex variables to estimate derivatives of real functions," *SIAM Review*, Vol. 40, 1998, pp. 110–112.

[57] Whitfield, D. and Taylor, L. K., "Variants of a two-level method for the approximate numerical solution of field simulation equations," Tech. rep., Computational Fluid Dynamics Laboratory, NSF Engineering Research Center for Computational Field Simulation, 1998.

[58] Wang, L., Anderson, W., Erwin, J., and Kapadia, S., "Solution of high-order methods for three-dimensional compressible viscous flows," *AIAA paper 2012-2836*, 2012.

[59] Saad, Y. and Schultz, M., "GMRES: A generalized minimal residual algorithm for solving nonsymmetric linear systems," *SIAM Journal on Scientific and Statistical Computing*, Vol. 7, 1986, pp. 856–869.

[60] Brufau, P., Vázquez-Cendón, M. E., and García-Navarro, P., "A numerical model for the flooding and drying of irregular domains," *International Journal for Numerical Methods in Fluids*, Vol. 39, 2002, pp. 247–275.

[61] Thacker, W. C., "Some exact solutions to the nonlinear shallow water wave equations," *Journal of Fluid Mechanics*, Vol. 107, 1981, pp. 499–508.

[62] Ippen, A. and Dawson, J., "Design of channel contractions, high-velocity flow in open channels: a symposium," *Transactions of the American Society of Civil Engineers*, Vol. 116, 1951, pp. 326–346.

[63] Stockstill, R. L. and Berger, R. C., "HIVEL2D: A two-dimensional two flow model for high-velocity channels," Tech. rep., REMR-HY-12, 1994.

[64] Whitfield, D. L., "Numerical solution of the shallow water equations," Tech. rep., NSF Engineering Research Center for Computational Field Simulation, 1996.

[65] Guo, W., Lai, J., Lin, G., Lee, F., and Tan, Y., "Finite-volume multi-stage scheme for advection-diffusion modeling in shallow water flows," *Journal of Mechanics*, Vol. 27, 2011, pp. 415–430.

[66] Takacs, L., "A two-step scheme for the advection equation with minimized dissipation and dispersion errors," *American Meteorological Society*, Vol. 113, 1985, pp. 1050–1065.

[67] Soares-Frazao, S., Noel, B., Spinewine, B., and Zech, Y., "The isolated building test case: results from the IMPACT benchmark," Tech. rep., Université Catholique de Louvain (UCL) Belgium, 2004.

VITA

Faranak Behzadi was born in ISFAHAN, IRAN, on March 30, 1984. After her elementary school, she was accepted to the exceptional talents school and studied Physics and Mathematics. She earned her Bachelor's degrees in Civil Engineering, and her Master's degree in Civil Engineering-Water Resources from the Isfahan University of Technology, ISFAHAN, IRAN. She received a Ph.D. in Computational Engineering from the University of Tennessee at Chattanooga in August 2016.